A&A 493, 89–105 (2009)
DOI: 10.1051/0004-6361:200810324

Astronomy & Astrophysics

The N_2D^+/N_2H^+ ratio as an evolutionary tracer of Class 0 protostars⋆

M. Emprechtinger[1], P. Caselli[2], N. H. Volgenau[1,⋆⋆], J. Stutzki[1], and M. C. Wiedner[1]

[1] Universität zu Köln, Zülpicher Str. 77, 50937 Cologne, Germany
e-mail: emprecht@ph1.uni-koeln.de
[2] School of Physics and Astronomy, University of Leeds, Leeds LS2 9JT, UK

Received 4 June 2008 / Accepted 16 September 2008

ABSTRACT

Context. Deuterated ions, especially H_2D^+ and N_2D^+, are abundant in cold (~10 K), dense (~10^5 cm^{-3}) regions, in which CO is frozen out onto dust grains. In such environments, the N_2D^+/N_2H^+ ratio can exceed the elemental abundance ratio of D/H by a factor of ≃10^4.

Aims. We use deuterium fractionation to investigate the evolutionary state of Class 0 protostars. In particular, we expect the N_2D^+/N_2H^+ ratio to decrease as temperature (a sign of the evolution of the protostar) increases.

Methods. We observed N_2H^+ 1–0, N_2D^+ 1–0, 2–1 and 3–2, $C^{18}O$ 1–0 and HCO^+ 3–2 in a sample of 20 Class 0 and borderline Class 0/I protostars. We determined the deuteration fraction and searched for correlations between the N_2D^+/N_2H^+ ratio and well-established evolutionary tracers, such as $T_{\rm Dust}$ and the CO depletion factor. In addition, we compared the observational result with a chemical model.

Results. In our protostellar sample, the N_2H^+ 1–0 optical depths are significantly lower than those found in prestellar cores, but the N_2H^+ column densities are comparable, which can be explained by the higher temperature and larger line width in protostellar cores. The deuterium fractionation of N_2H^+ in protostellar cores is also similar to that in prestellar cores. We found a clear correlation between the N_2D^+/N_2H^+ ratio and evolutionary tracers. As expected, the coolest, i.e. the youngest, objects show the largest deuterium fractionation. Furthermore, we find that sources with a high N_2D^+/N_2H^+ ratio show clear indications of infall (e.g. $\delta v < 0$). With decreasing deuterium fraction, the infall signature disappears and δv tends to be positive for the most evolved objects. The deuterium fractionation of other molecules deviates clearly from that of N_2H^+. The DCO^+/HCO^+ ratio stays low at all evolutionary stages, whereas the NH_2D/NH_3 ratio is >0.15 even in the most evolved objects.

Conclusions. The N_2D^+/N_2H^+ ratio is known to trace the evolution of prestellar cores. We show that this ratio can be used to trace core evolution even after star formation. Protostars with an N_2D^+/N_2H^+ ratio above 0.15 are in a stage shortly after the beginning of collapse. Later on, deuterium fractionation decreases until it reaches a value of ~0.03 at the Class 0/I borderline.

Key words. ISM: clouds – ISM: evolution – ISM: molecules – stars: formation

1. Introduction

Early attempts to describe an evolutionary sequence of protostars classified them according to their near- and mid-infrared spectra. Lada & Wilking (1984) divided a sample of protostellar sources in the ρ Ophiuchi cloud into three classes (Class I to III with progressive evolutionary stage). André et al. (1993) introduced the Class 0 stage. The strong submillimetre emission of Class 0 objects relative to their bolometric luminosity suggests that the mass of the circumstellar envelope is higher than the mass of the central star. Class 0 objects are the youngest among the protostars. In subsequent years, more sensitive indicators for protostar evolution were established, such as the bolometric temperature (Myers & Ladd 1993), the $L_{\rm BOL}/L_{\rm smm}$ ratio (André et al. 1993) and the correlation between the bolometric luminosity and the distance normalised 1.3 mm flux (Saraceno et al. 1996). All these evolutionary indicators are based on the change of the spectral energy distribution (SED) of the protostar. As it heats up, an increasing fraction of the radiation is emitted at shorter wavelengths, leading to an increase in $L_{\rm BOL}$ and $T_{\rm BOL}$ with time.

Several theoretical models connect physical properties of the protostars with the time since gravitational collapse (e.g. Smith 1998; Myers et al. 1998). However, although the evolutionary stages determined by different models is the same (i.e. the time sequence is the same), the absolute ages vary significantly. The absolute age for Class 0/I borderline objects, for example, varies between 10^4 and a few times 10^5 years (Froebrich 2005). In this paper, we show that it is possible to use the deuterium fractionation of N_2H^+ as an evolutionary tracer.

The chemistry of cold ($T < 20$ K), dense ($n = 10^5$ cm^{-3}) environments in space is peculiar. Common molecular tracers, such as CO and CS, appear reduced in abundance because they freeze out onto dust grains (e.g. Willacy et al. 1998; Caselli et al. 1999; Kramer et al. 1999; Bergin et al. 2002; Redman et al. 2002; Tafalla et al. 2002, 2004). By comparison, molecules such as N_2H^+ and NH_3 suffer less from depletion. The persistence of nitrogen-bearing species likely stems from the fact that N_2, the progenitor of these species, remains in the gas phase longer than CO, despite laboratory measurements finding that the binding energy, as well as the sticking coefficient of N_2 and CO on dust, are quite similar (Öberg et al. 2005;

⋆ Based on observations with the IRAM 303 m telescope.
⋆⋆ *Current address*: California Institute of Technology, Owens Valley Radio Observatory, Big Pine, CA 93513 USA.

Bisschop et al. 2006). Recent theoretical work suggests that the resistance of nitrogen-bearing species to depletion may come from a significant fraction of interstellar nitrogen being in atomic (N) rather than molecular (N_2) form (Maret et al. 2006; Flower et al. 2006). Atomic nitrogen has a lower binding energy than molecular nitrogen and CO.

One consequence of the low temperatures and freeze-out of CO in pre- and protostellar cores is that the abundance of deuterated molecules is greatly enhanced. In such regions, column density ratios for N_2D^+/N_2H^+ of 0.24 (Caselli et al. 2002b), $D_2CO/H_2CO \simeq 0.01-0.1$ (Bacmann et al. 2003), NH_2D/NH_3 up to 0.33 (Hatchell 2003), and DCO^+/HCO^+ in the order of 0.01 (Jørgensen et al. 2004) are found. These ratios are three to four orders of magnitudes over the average ISM D/H ratio of 1.5×10^{-5} (Oliveira et al. 2003). Models show that the abundance of H_2D^+, a fundamental molecule in deuterium chemistry, rises steeply as temperature decreases (e.g. Flower et al. 2004; Roberts & Millar 2000). Consequently, the deuterium fractionation of many other molecules also increases (Millar et al. 2000).

In a recent study, Crapsi et al. (2005) investigated the N_2D^+/N_2H^+ ratio in 31 low-mass *starless cores* and finds ratios in the range of a few percent to 0.44. They also find a tight correlation between the N_2D^+/N_2H^+ ratio and the CO depletion factor; the ratio is greater where CO is depleted. Furthermore, they attempted to find correlations between the N_2D^+/N_2H^+ ratio and various chemical and dynamical evolutionary indicators (e.g. core density, molecular column density, line width, and line asymmetry). Although the dependencies on particular indicators are not always clear, they identified a recognisable trend. The N_2D^+/N_2H^+ ratio was generally found to increase as a cloud core evolves towards the moment of protostellar collapse. Another result of their work is that the trends seen in the subsample of Taurus cores were more homogeneous than trends in the total sample. This homogeneity led them to speculate that a core's external environment plays an important role in its evolution. In this work we follow the trend of the N_2D^+/N_2H^+ ratio to the subsequent, early protostellar stages.

One recent study that also sought to determine the behaviour of deuterated molecules in protostellar environments is from Roberts & Millar (2007). They determine the N_2D^+/N_2H^+ ratio in five low-mass *protostellar cores*, using the University of Arizona 12 m telescope (*HPBW* of 70″ for N_2H^+ 1–0). Furthermore they measured the D_2CO/H_2CO and the $HDCO/H_2CO$ ratio in these cores. The $HDCO/H_2CO$ ratio was similar in most cores (~0.06), with the exception of the object with the highest N_2D^+/N_2H^+ ratio, where $HDCO/H_2CO$ was lowest. For four sources, the N_2D^+/N_2H^+ ratio appeared anti-correlated with the D_2CO/H_2CO ratio. Only in L 1527 were both N_2D^+ and D_2CO abundances anomalously low. They did not find a correlation between deuterium fractionation and bolometric temperature for any of the observed molecules. However, due to the small number of protostars, this work cannot rule out any trend of the deuterium fractionation in protostellar cores.

We observed 20 Class 0 protostars in N_2H^+ and N_2D^+, using the IRAM 30 m telescope (*HPBW* of 27″ for N_2H^+ 1–0, see Sect. 2). The goal of our study is to investigate the trend in deuterium fractionation after the moment of star formation. Spectra and line parameters are presented in Sect. 3. We expect that the N_2D^+/N_2H^+ ratio (determined in Sect. 4.1) should decrease during protostellar evolution due to the internal heating of the core. As the core environment warms up, H_2D^+ and its more highly deuterated isotopologues are destroyed. Consequently, all other deuterated molecules formed by reactions with H_2D^+ (such as N_2D^+) are destroyed as well. In Sect. 4.2- 4.4, the N_2D^+/N_2H^+ ratio is compared with evolutionary indicators, namely dust temperature, CO depletion factor, and $L_{BOL}/F_{1.3}$. Possible correlations with kinematical parameters of the gas are investigated in Sect. 4.5. In addition, we compare the N_2D^+/N_2H^+ ratio with the deuterium fractionation of other molecules (Sect. 4.6). Finally, we compare our results with the predictions of a simple chemical model (Sect. 5).

Table 1. Class 0 objects observed for the survey.

Source	RA (J2000.0)	Dec (J2000.0)	Distance [pc]
L 1448 IRS 2	03:25:22.4	30:45:12	220[1]
L 1448 IRS 3	03:25:36.4	30:45:20	220[1]
L 1448 C	03:25:38.8	30:44:05	220[1]
L 1455 A1	03:27:42.1	30:12:43	220[1]
L 1455 A2	03:27:49.8	30:11:42	220[1]
Per 4 S	03:29:17.9	31:27:30	220[1]
Per 4 N	03:29:22.7	31:33:30	220[1]
Per 5	03:29:51.6	31:39:03	220[1]
Per 6	03:30:14.8	30:23:48	220[1]
IRAS 03282+3035	03:31:21.0	30:45:30	220[1]
Barnard 1-b	03:33:21.3	31:07:35	220[1]
HH 211	03:43:56.8	32:00:50	220[1]
Barnard 5 IRS1	03:47:41.6	32:51:42	220[1]
L 1527	04:39:53.5	26:03:05	140[2]
L 483	18:17:29.8	–04:39:38	200[2]
SMM 5	18:29:51.2	01:16:40	310[3]
L 723	19:17:53.1	19:12:16	300[2]
L 673 A	19:20:25.8	11:19:51	300[2]
B 335	19:37:01.4	07:34:06	250[2]
L 1157	20:39:06.5	68:02:13	440[4]

[1] Černis (1990); [2] Jijina et al. (1999); [3] Froebrich (2005); [4] Gueth et al. (2003).

2. Observations

2.1. Source sample

Our survey includes 20 Class 0 protostellar cores. Table 1 lists the objects, their coordinates, and their estimated distances. The sources were selected in terms of being a) well known (i.e. many complementary data can be found in the literature) and b) representing a range of stages of Class 0 sources, from very young objects (e.g. HH 211, which is one of the youngest protostars according to Froebrich 2005) to borderline objects (Class 0/1), such as L1455 A1 (Froebrich 2005) and Barnard 5 IRS 1 (Velusamy & Langer 1998). For one object, L 1527, the classification is ambiguous. The continuum data denote it as a Class 0 object, but an embedded source is detected at a wavelength <5 μm (Froebrich 2005), indicating that this protostar is already more evolved. Therefore, this source is also classified as a Class 0/I borderline object. Most of the objects (13) are located in the Perseus molecular cloud, and all are at a distance closer than 500 pc. For the sources located in Perseus, we assumed a distances of 220 pc (Černis 1990). Other authors (e.g. Herbig & Jones 1983) give distances greater than 300 pc. Eleven objects belong to a sample of sources catalogued by Froebrich (2005), and for 17 sources, kinetic gas temperatures are known from NH_3 observations (Jijina et al. 1999). However, the NH_3 observations vary in spatial resolution between 40″ and 80″. To avoid systematic errors, introduced by the different beam sizes, we use these kinetic temperatures here only to estimate the gas temperature.

Table 2. Observed emission lines.

Line	Frequency [GHz]	*HPBW* [″]
N_2D^+ 1–0	77.109	32
N_2H^+ 1–0	93.173	27
$C^{18}O$ 1–0	109.782	22
N_2D^+ 2–1	154.217	16
N_2D^+ 3–2	231.322	11
HCO^+ 3–2	267.558	10

2.2. Molecular line observations

The observations were carried out in January 2006 using the IRAM-30 m telescope. In Table 2, the molecular line transitions, their frequencies, and their corresponding half-power beam widths (*HPBW*) are given. Two different receiver set-ups were used. The first set-up used frequency switching to observe $C^{18}O$ 1–0, N_2D^+ 2–1, N_2D^+ 3–2, and HCO^+ 3–2 simultaneously. The offsets were 10 ($C^{18}O$ 1–0), 15 (N_2D^+ 2–1), 25 (N_2D^+ 3–2), and 28 (HCO^+ 3–2) MHz, respectively. The second set-up used an external local oscillator to observe the N_2D^+ 1–0 line. In this mode, frequency switching was not available, so position switching was used instead. The N_2D^+ 1–0 line was observed simultaneously with the N_2H^+ 1–0 and N_2D^+ 3–2 lines. As a back end, the VESPA autocorrelator was used, which was adjusted to a resolution of about 0.05 km s^{-1} at each frequency.

During observations, the atmospheric τ(225 GHz) was about 0.25, which is a typical opacity for winter weather conditions at the IRAM site. The corresponding system temperatures were between 150 K (N_2H^+ 1–0) and 800 K (HCO^+ 3–2). Pointing was checked every two hours, and the pointing accuracy was better than 3″. Antenna temperatures and main beam temperatures are related by the main beam efficiency, η_{MB}, which is between 0.8 and 0.42, depending on the observing frequency[1].

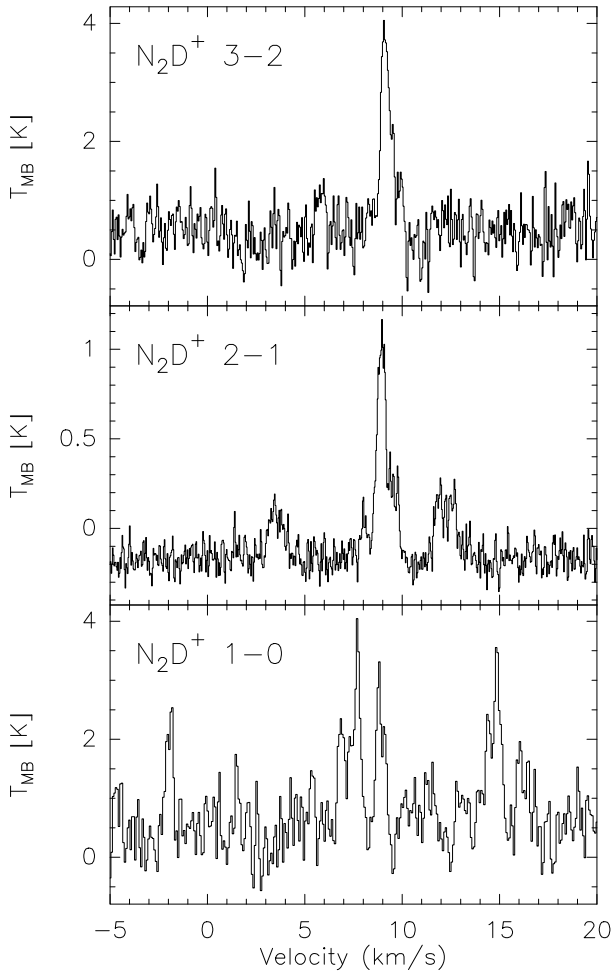

Fig. 1. Spectra of N_2D^+ 1–0, N_2D^+ 2–1, and N_2D^+ 3–2 toward HH 211, one of the youngest sources in our sample.

3. Results

3.1. N_2H^+ and N_2D^+

The results of the N_2H^+ and N_2D^+ observations are summarised in Table 3. Figure 1 shows the three N_2D^+ transitions observed toward HH 211, one of the few sources (total of 6, see Table 3) where all lines are detected. The N_2H^+ 1–0, N_2D^+ 2–1, $C^{18}O$ 1–0, and HCO^+ 3–2 spectra of all 20 sources are displayed in Fig. 2.

The N_2H^+ 1–0 line was detected in all sources of our sample. The total optical depth was determined by fitting all hyperfine components of the line using the "METHOD HFS" of the CLASS program[2]. The relative intensities of the hyperfine components given by Womack et al. (1992) were assumed. With the exception of Per 6, the line optical depths could be determined with at least 3.5σ in all objects (see Table 3). T_{ex} was estimated using the equation

$$T_{MB} = (J(T_{ex}) - J(T_{BG})) \cdot (1 - e^{-\tau})$$

where T_{ex} is the excitation temperature, T_{BG} the cosmic background temperature (2.7 K), and $J(T) = [h\nu/k]/[\exp(h\nu/kT) - 1]$. In most cases, the excitation temperature of N_2H^+ is lower than the kinetic gas temperature listed in Jijina et al. (1999) and Hatchell (2003), most likely due to line-of-sight average volume densities of the emitting gas lower than the critical density of the observed transitions ($\simeq 10^5$ cm^{-3} for N_2H^+(1–0)). The factor by which T_{ex} is lower than T_{kin} varies from source to source from close to 1 (L 1448 IRS 3) to 0.43 (HH 211). However, these excitation temperatures are typically 2–3 K higher than those in the prestellar cores observed by Crapsi et al. (2005). Another contrast with the prestellar cores is that none of the lines in our sample show highly non-Gaussian profiles.

The N_2H^+ 1–0 line widths found in our protostellar sample are significantly larger than the ones in prestellar cores. The average line width for our sample is 0.61 km s^{-1}, whereas Crapsi et al. (2005) find an average line width of 0.26 km s^{-1}. The line widths reported by Roberts & Millar (2007) are slightly broader than ours (0.85 km s^{-1}), but this difference might be due to the lower spatial resolution of their observations. This suggests that nonthermal motions are not only concentrated nearby the protostar, but also that they pervade the whole associated envelope, increasing outward as commonly found in molecular cloud cores (e.g. Fuller & Myers 1992).

N_2D^+ was observed in three different transitions (J = 1–0, J = 2–1 and J = 3–2). All three lines were detected in six objects. The ground-state transition, N_2D^+ 1–0, was detected in only seven sources, but the S/N of four of these is too low to obtain a reliable τ from hyperfine component fitting. Only in L 1448 IRS 3 and Barnard 1-b is the line strong enough, and the HFS method yielded τ = 1.3 ± 0.4 and 0.9 ± 0.2, respectively. The reason for the rarity of N_2D^+ 1–0 detections is that the

[1] http://www.iram.fr/
[2] http://www.iram.fr/IRAMFR/GILDAS/

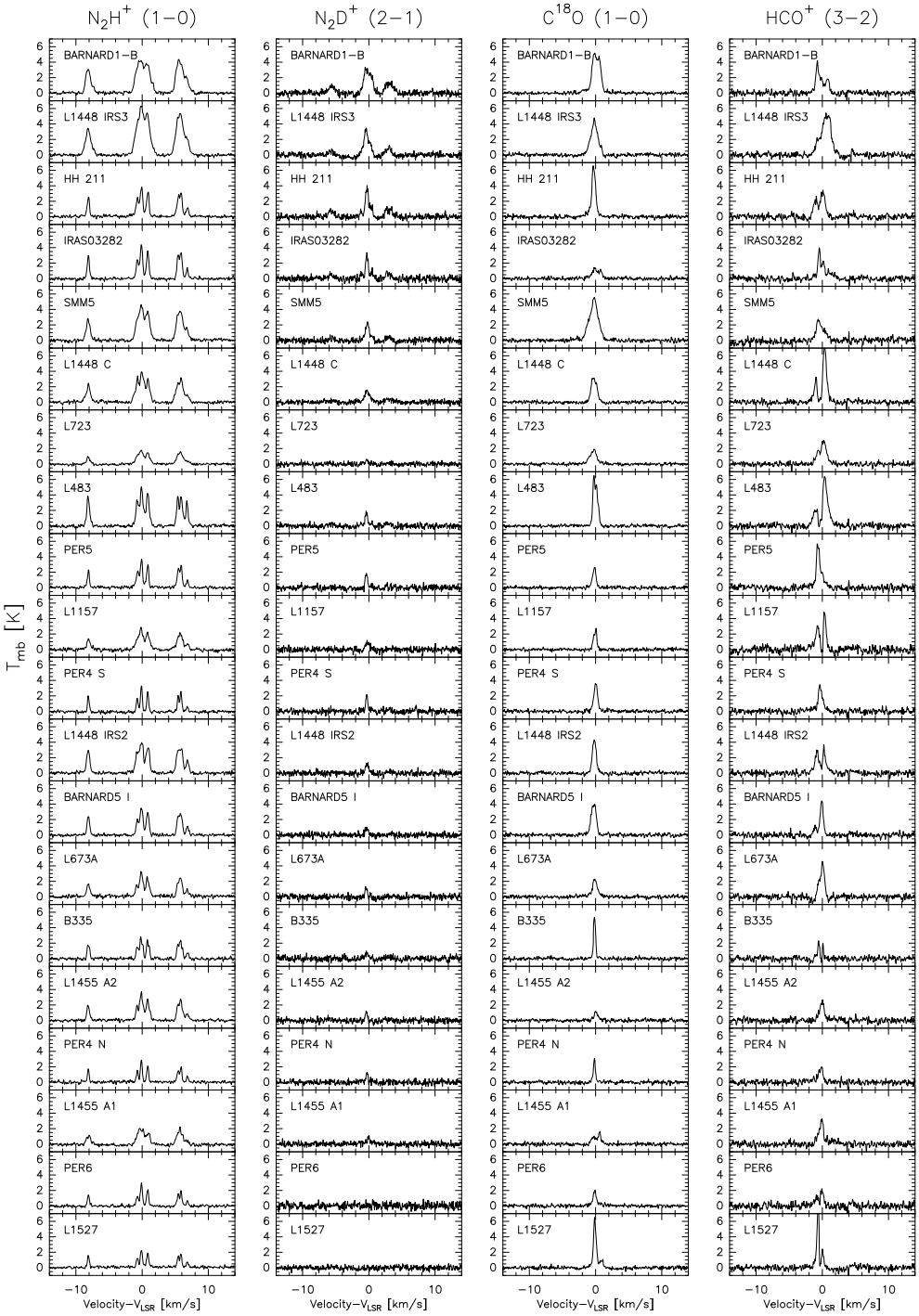

Fig. 2. Spectra of N_2H^+ 1–0, N_2D^+ 2–1, $C^{18}O$ 1–0, and HCO^+ 3–2 (*from left to right*) of all 20 protostars of our sample. To be able to plot all spectra in one plot, we divided the intensities of HCO^+ by three.

Einstein-A coefficient, i.e. the transition probability, increases with $\sim J^3$, and thus the A-coefficient for the $J = 1–0$ line is ten times lower than the A-coefficient of the $J = 2–1$ line. Furthermore, the relatively low energies ($E = J(J+1) \cdot 1.85$ K) and the higher degeneracies of higher rotational states lead to an efficient population of those states under conditions present in protostellar cores ($n \simeq 10^5$ cm^{-3}, $T = 10–20$ K).

The 2–1 line is the most frequently detected N_2D^+ line. Only two objects, Per 6 and L 1527, do not show emission in $J = 2–1$. These two objects also show no emission in the other N_2D^+ lines. In most cases, the $J = 2–1$ lines are optically thin, so that τ can be determined by fitting the hyperfine components in only five cases.

The N_2D^+ 3–2 line is detected in 15 out of the 20 cores. Because the satellite lines get weaker with increasing J, and due to the higher noise-level of most of these data, it was not possible to derive reliable optical depths.

The integrated intensities of the N_2H^+ 1–0 lines from the cores in our sample are comparable to the intensities found in prestellar cores (Crapsi et al. 2005), but the optical depths in the protostellar cores are typically lower by a factor of three. The integrated intensity and optical depth of N_2D^+ 2–1

Table 3. Line parameters of the N_2H^+ and N_2D^+ lines.

Source	N_2H^+ (1–0)					N_2D^+					
	W [K km s^{-1}]	Δv [km s^{-1}]	τ	T_{ex} [K]	T_{Kin} [K]	$W_{J=1-0}$ [K km s^{-1}]	$W_{J=2-1}$ [K km s^{-1}]	$W_{J=3-2}$ [K km s^{-1}]	τ $J=2-1$	Δv_{2-1} [km s^{-1}]	T_{ex} [K]
L 1448 IRS 2	12.93	0.50	11.6	6.8	–	1.7	1.10	0.73	<0.1	0.53	–
L 1448 IRS 3	24.65	0.93	4.1	11.4	12.0	4.0	5.05	3.22	2.6	0.59	7.9
L 1448 C	12.48	0.76	5.3	7.3	13.7*	<1	2.32	1.38	<0.1	0.72	–
L 1455 A1	7.20	0.74	1.4	9.2	15.0	<1	0.68	<0.74	<0.1	0.42	–
L 1455 A2	8.60	0.54	3.0	9.1	11.0	<1	1.03	<0.73	<0.1	0.33	–
Per 4 S	5.08	0.29	3.5	8.5	9.0	1.3	1.43	0.98	<0.1	0.32	–
Per 4 N	4.62	0.31	3.6	7.6	10.0	1.3	0.75	<0.68	<0.1	0.31	–
Per 5	7.53	0.38	3.8	8.7	11.0	<1	1.07	1.08	<0.1	0.36	–
Per 6	4.64	0.36	<0.1	–	11.0	<1	<0.18	<0.69	–	–	–
IRAS 03282	9.53	0.38	5.3	8.6	11.3*	<1	3.58	1.47	3.9	0.34	7.9
Barnard 1-B	19.05	0.82	8.6	7.6	12.0	5.9	7.48	4.82	4.9	0.78	6.7
HH 211	9.18	0.41	6.2	7.6	12.8*	2.3	5.24	2.08	4.9	0.39	7.5
Barnard 5 IRS 1	8.59	0.43	6.4	7.2	10.8*	<1	0.50	0.65	<0.1	0.50	–
L 1527	3.91	0.32	5.6	5.7	10.8*	<1	<0.18	<0.59	–	–	–
L 483	14.05	0.44	12.1	7.3	10.0	2.1	1.75	1.13	2.8	0.37	5.5
SMM 5	15.39	0.70	4.9	8.9	12.0	<1	2.46	1.43	<0.1	0.58	–
L 723	5.70	0.71	2.4	6.6	11.0	<1	0.34	1.29	<0.1	0.32	–
L 673 A	7.34	0.54	2.9	8.6	<12.0	<1	0.45	0.63	<0.1	0.34	–
B 335	6.05	0.40	9.0	5.7	9.9	<1	0.42	0.42	<0.1	0.46	–
L 1157	8.38	0.65	2.1	8.9	–	<1	0.53	1.00	<0.1	0.56	–

The kinetic gas temperatures marked with an * are taken from Hatchell (2003). All other T_{kin} values are listed in Jijina et al. (1999). The errors on the integrated intensities of N_2H^+ 1–0 and N_2D^+ 2–1 are ∼10% (calibration uncertainties), whereas the errors on the N_2D^+ 1–0 and N_2D^+ 3–2 lines are dominated by the noise of the spectra (0.5 and 0.2 K km s^{-1} for $J = 1-0$ and $J = 3-2$, respectively). τ is the total optical depth, defined as the sum of the optical depths of the individual hyperfine components. Typical errors of τ are ±0.5 and ±0.2 for N_2H^+ and N_2D^+ 2–1 (where it is detected), respectively. The resulting error of T_{ex} is ∼0.2 K for both species.

are approximately the same in pre- and protostellar cores, but N_2D^+ 3–2 is significantly stronger in the latter (∼0.3 K km s^{-1} and ∼1.42 K km s^{-1}, respectively).

3.2. $C^{18}O$ and HCO^+

The $C^{18}O$ 1–0 and HCO^+ 3-2 lines were detected in all 20 sources of our sample. The line parameters are listed in Table 4. The line profile of $C^{18}O$, which is assumed to be optically thin, looks roughly Gaussian. The only two exceptions are L 1455 A1 and IRAS 03282, which show more complex line shapes, indicating that these sources may contain several velocity components. The $C^{18}O$ line width (*FWHM*) is quite narrow, typically <1 km s^{-1}. Such narrow line widths indicate that the bulk of the molecular gas is cold, and turbulence is low. The column densities we calculated for $C^{18}O$ (see below), indicate that the C^{18} 1–0 line is optically thin in these objects.

The line shape of HCO^+ 3–2 deviates clearly from a Gaussian profile. Double-peaked profiles appear in 12 objects, with minima at the position of the optically thin $C^{18}O$ emission, a clear indication of self-absorption. Asymmetries in the line shape indicate a systematic velocity pattern, which is probably caused by infall motions.

Gregersen et al. (2000) observed several young protostars in HCO^+ 3–2 using the Caltech Submillimeter Observatory (CSO). They found line shapes that show similar asymmetries to those we detect (see Sect. 4.5), but the intensities of the lines they observed are significantly lower. This discrepancy is most likely caused by the larger beam size (32.5″) of the CSO at 268 GHz. For three sources common to the Gregersen et al. (2000) study and ours, we determined beam filling factors based on the HCO^+ 3–2 lines. We used a CSO beam efficiency of 69.8% at 269 GHz to convert their T_A^* to T_{MB}. Assuming that HCO^+ 3–2 is emitted from a small region at the centre of the core, as suggested by our models (see Sect. 5.4), we estimated the size of this region by comparing the T_{MB} ratio to the ratio of the beam size of the two observations. The derived filling factors for the CSO observations were between 0.26 and 0.36, yielding a diameter of the warm nucleus of approximately 4000 AU. Contributions of the error beams to the IRAM observations have been neglected here, but because of the small size of the HCO^+ emitting region means their contribution is <1%.

Table 4. Observational parameters of the $C^{18}O$ and HCO^+ lines.

Source	W [K km s^{-1}] ($C^{18}O$)	Δv [km s^{-1}] ($C^{18}O$)	W [K km s^{-1}] (HCO^+)
L 1448 IRS 2	3.23 ± 0.05	0.77 ± 0.01	13.0 ± 0.3*
L 1448 IRS 3	5.75 ± 0.07	1.22 ± 0.01	29.0 ± 0.3
L 1448 C	3.36 ± 0.06	1.11 ± 0.01	20.6 ± 0.3*
L 1455 A1	1.65 ± 0.06	1.03 ± 0.01	8.8 ± 0.3
L 1455 A2	0.90 ± 0.05	0.80 ± 0.01	6.5 ± 0.3
Per 4 S	2.84 ± 0.06	0.81 ± 0.01	8.7 ± 0.3
Per 4 N	1.30 ± 0.04	0.44 ± 0.01	5.3 ± 0.3
Per 5	1.79 ± 0.05	0.69 ± 0.01	15.0 ± 0.3
Per 6	1.52 ± 0.05	0.74 ± 0.01	6.1 ± 0.3*
IRAS 03282	1.95 ± 0.07	1.47 ± 0.01	12.8 ± 0.3*
Barnard 1-B	8.09 ± 0.08	1.59 ± 0.01	14.0 ± 0.3*
HH 211	5.19 ± 0.06	0.81 ± 0.01	17.4 ± 0.3*
Barnard 5 IRS 1	3.99 ± 0.06	1.00 ± 0.01	9.3 ± 0.3*
L 1527	4.12 ± 0.06	0.65 ± 0.01	13.0 ± 0.3*
L 483	5.12 ± 0.06	0.81 ± 0.01	22.8 ± 0.3*
SMM 5	8.66 ± 0.08	1.57 ± 0.01	10.7 ± 0.3
L 723	2.45 ± 0.08	1.29 ± 0.01	12.2 ± 0.3*
L 673 A	2.31 ± 0.07	0.92 ± 0.01	12.8 ± 0.3
B 335	2.34 ± 0.04	0.44 ± 0.01	3.6 ± 0.3*
L 1157	1.57 ± 0.05	0.61 ± 0.01	13.4 ± 0.3*

Integrated HCO^+ intensities from double-peaked spectra are indicated with an *.

4. Analyses

In this section, we calculate the N_2D^+/N_2H^+ ratios and correlate them with physical parameters of the protostars that might influence deuterium fractionation. Some of these parameters, such as dust temperature and bolometric luminosity, can be used to quantify the evolutionary stage of the protostar. Each parameter will be discussed in individual subsections.

4.1. N_2H^+ and N_2D^+ volume densities, column densities and deuterium fractionation

To derive the deuterium enhancement, one calculates the ratio of the column densities of a hydrogen-bearing species and its deuterated isotopologue. Many common C-bearing molecules (e.g. HCO^+ and H_2CO) suffer from depletion in cold and dense environments (see Tafalla et al. 2006), and thus the deuterated species trace slightly warmer regions of the core, where the parent molecules are not depleted. To properly determine the deuterium fractionation of an entire core, one has to observe molecules that are less affected by depletion, such as N_2H^+ and NH_3. Another benefit of observing N-bearing molecules is that their emission lines split into hyperfine components due to the non-zero nuclear spin of nitrogen, enabling optical depths to be measured.

To determine molecular column densities, we used the N_2H^+ 1−0 and N_2D^+ 2−1 lines. We chose these lines for three reasons. First, N_2D^+ 2−1 is detected in most of the sources. Second, the 2−1 transition of N_2D^+ is observed with the highest S/N. Third, the ratio of the N_2D^+ 2−1/N_2H^+ 1−0 lines permits a direct comparison with previous studies (Crapsi et al. 2005; Fontani et al. 2006). The column densities were derived (Table 5) by assuming a constant excitation temperature, as determined in Sect. 3 (CTEX-method, for details see the appendix of Caselli et al. 2002b). The excitation temperature of N_2H^+ can be determined in all objects but Per 6 (Table 3), where the N_2H^+ line is optically thin. For Per 6, we assumed an excitation temperature of 8 K, which is the mean excitation temperature of the sample. The situation is different for N_2D^+, since the N_2D^+ 2−1 line is optically thin in most objects. In the few sources where τ could be determined, the excitation temperatures of N_2H^+ and N_2D^+ were approximately the same. In all cases where the excitation temperature of N_2D^+ was unknown, we assumed that it was the same as for N_2H^+. The estimated errors on the column densities are approximately 15% and 20% for N_2H^+ and N_2D^+, respectively. As expected, the N_2D^+/N_2H^+ ratios vary significantly from object to object (Table 5). The extreme values are <0.029 for Per 6 and 0.27 for HH 211. For most objects, the ratio is below 0.1.

Determining T_{ex} and the column densities as described above, we implicitly assume a unity beam-filling factor for the N_2H^+ and N_2D^+ observations. Because dark cloud cores are typically larger than the beam size of our observations (e.g. Caselli et al. 2002a) and because the kinetic temperature of these cores is only ∼1.5 times, the excitation temperature of N_2H^+ indicates that the filling factor is indeed close to one, and certainly >0.67. Using the lower limit for the filling factor would lower the N_2H^+ column density by 40% and the N_2D^+ column density by 55%. Therefore, the derived N_2D^+/N_2H^+ ratios could be up to 25% lower. The general trend, however, remains and will be discussed in the next section.

The N_2D^+ column density was also calculated using the (3−2) line, where detected, following the same procedure as described above. In 13 out of 15 objects, the values for the column density agree within the range of error. In L 1448 IRS3 and L 1157, the column densities determined using N_2D^+ 3−2 are a factor of two higher than those determined using the 2−1 line. However, because of the lower S/N of the N_2D^+ 3−2 line, the column densities determined using the J = 2−1 transition are more reliable.

Table 5. N_2H^+ and N_2D^+ column densities.

Source	$N(N_2H^+)$ [cm^{-2}]	$N(N_2D^+)$ [cm^{-2}]	$N(N_2D^+)/N(N_2H^+)$
L 1448 IRS 2	3.1×10^{13}	1.3×10^{12}	0.042 ± 0.014
L 1448 IRS 3	4.8×10^{13}	3.9×10^{12}	0.081 ± 0.010
L 1448 C	2.4×10^{13}	2.5×10^{12}	0.104 ± 0.017
L 1455 A1	9.2×10^{12}	6.3×10^{11}	0.068 ± 0.043
L 1455 A2	1.4×10^{13}	9.6×10^{11}	0.069 ± 0.029
Per 4 S	7.9×10^{12}	1.4×10^{12}	0.177 ± 0.032
Per 4 N	7.1×10^{12}	7.8×10^{11}	0.110 ± 0.057
Per 5	1.2×10^{13}	1.0×10^{12}	0.083 ± 0.033
Per 6	6.1×10^{12}	$<1.8 \times 10^{11}$	<0.029
IRAS 03282	1.6×10^{13}	3.5×10^{12}	0.219 ± 0.026
Barnard 1-B	4.5×10^{13}	8.1×10^{12}	0.180 ± 0.009
HH 211	1.7×10^{13}	4.6×10^{12}	0.271 ± 0.024
Barnard 5 IRS 1	1.6×10^{13}	5.4×10^{11}	0.034 ± 0.025
L 1527	7.2×10^{12}	$<2.5 \times 10^{11}$	<0.034
L 483	3.3×10^{13}	1.9×10^{12}	0.057 ± 0.012
SMM 5	2.9×10^{13}	2.3×10^{12}	0.079 ± 0.019
L 723	8.8×10^{12}	4.0×10^{11}	0.045 ± 0.040
L 673 A	1.3×10^{13}	4.3×10^{11}	0.033 ± 0.031
B 335	1.4×10^{13}	6.0×10^{11}	0.043 ± 0.029
L 1157	1.1×10^{13}	5.0×10^{11}	0.045 ± 0.036

Estimated errors on the column densities are about 15% and 20% for N_2H^+ and N_2D^+, respectively.

The N_2H^+ and N_2D^+ column densities derived here are comparable to those found by Crapsi et al. (2005) for prestellar cores (10^{13} cm^{-2} and 10^{12} cm^{-2} for N_2H^+ and N_2D^+, respectively).This result is somewhat unexpected, because the optical depth of N_2H^+ is about three times lower in protostars than in prestellar cores. However, the higher excitation temperatures and broader line widths of N_2H^+ in protostellar envelopes (over-)compensate for the lower optical depth. The range of values for the N_2D^+/N_2H^+ ratio is also similar. The average ratio in our sample of Class 0 protostars is 0.097, and 20% of the objects have a ratio greater than 0.15. For starless cores, the average ratio is 0.106, and 18% of the sources have ratios above 0.15. However, the N_2D^+/N_2H^+ ratio in both protostellar and prestellar cores is significantly larger than the ratio in high mass star-forming regions (always less than 0.02, Fontani et al. 2006), although values as high as 0.1 have been measured with interferometric observations (Fontani et al. 2008).

For three objects in our sample, L 1448 C, HH 211, and L 1527, N_2D^+/N_2H^+ was also determined by Roberts & Millar (2007). In general, they find somewhat higher N_2D^+/N_2H^+ ratios than we do. In L 1448 C, their ratio is 1.63 ± 0.4 times greater. In HH 211, their ratio is 1.14 ± 0.18 times greater. For L 1527, we report an upper limit of 0.034, whereas Roberts & Millar found a ratio of 0.06. That Roberts & Millar (2007) found similar N_2D^+/N_2H^+ ratios at much lower spatial resolution indicates that the deuterium fractionation occurs, as expected, in the cold, extended envelope of the protostellar core. If deuterium fractionation occurred only in the central region, one would expect beam dilution to yield lower N_2D^+/N_2H^+ at lower resolutions.

Table 6. Continuum observations and derived properties (dust temperature, $C^{18}O$ column density, CO depletion factor) for sources in our survey.

Source	IRAS	$F(60\ \mu m)$ [Jy]	$F(100\ \mu m)$ [Jy]	Wavelength of additional data [μm]	T_{Dust} [K]	$N(C^{18}O)$ [cm^{-2}]	$f_D(CO)$
L 1448 IRS 2	03222+3034	14.3	<169	450, 850, 1100[1,3]	27	6.07×10^{15}	2.6 ± 0.6
L 1448 IRS 3	03225+3034	25.1	169	1100[3]	27	1.08×10^{16}	4.4 ± 1.0
L 1448 C	F03226+3033	53.4	355	450, 850, 1100[2,3]	32	$7.18.19 \times 10^{15}$	2.8 ± 0.6
L 1455 A1	03245+3002	47.1	93.6	1100, 450, 850[3,5]	37	3.53×10^{15}	1.5 ± 0.4
L 1455 A2	F03247+3001	66.4	206	–	30	1.83×10^{15}	–
Per 4 S	–	–	–	1100[3]	–	3.18×10^{15}	–
Per 4 N	03262+3123	1.07	<12.4	1100[3]	23	2.18×10^{15}	2.4 ± 0.11
Per 5	03267+3128	1.88	<10.4	1100[3]	26	3.28×10^{15}	1.6 ± 0.4
Per 6	03271+3013	7.53	8.19	–	45	4.28×10^{15}	–
IRAS 03282	03282+3035	2.33	13.9	450, 850, 1100[2,3]	23	3.28×10^{15}	3.9 ± 0.9
Barnard 1-B	03301+3057	<6.18	35.5	1100, 850[3,4]	18	1.16×10^{16}	2.9 ± 0.7
HH 211	03407+3152	<2.06	<30.8	1100, 450, 850[3,5]	<21	8.21×10^{15}	2.9 ± 0.7
Barnard 5 IRS 1	03445+3242	15.5	15.4	1100[3]	50	1.23×10^{16}	0.3 ± 0.09
L 1527	04368+2557	17.8	73.3	450, 850, 1300[2]	27	7.75×10^{15}	2.3 ± 0.5
L 483	18148-0440	89.1	166	450, 850[2]	34	1.15×10^{16}	2.1 ± 0.5
SMM 5	–	–	–	–	–	9.70×10^{15}	–
L 723	19156+1906	6.93	20.7	450, 850[2]	25	4.36×10^{15}	2.9 ± 0.7
L 673 A	19180+1114	2.55	10.6	–	28	4.47×10^{15}	–
B 335	19345+0727	8.3	42	450, 850, 1300[2]	27	4.41×10^{15}	3.3 ± 0.8
L 1157	20386+6751	10.9	43.5	1300, 450, 850[2,5]	30	3.19×10^{15}	4.2 ± 1.0

The errors in the dust temperatures are ~2 K, and the $C^{18}O$ column densities are accurate to 10%.
References: [1] O'Linger et al. (1999); [2] Shirley et al. (2000); [3] Enoch et al. (2006); [4] Hatchell et al. (2005); [5] Froebrich et al. (2003).

We also estimated the volume densities of the cores. Because the N_2D^+ lines show only a single velocity component, we used the ratios of the integrated intensities of these lines instead of the T_{MB} ratios. Thus we obtained a higher S/N. Further we assumed an isothermal cloud with a kinetic temperature determined from NH_3 observations (Table 3). The volume density was estimated by fitting the N_2D^+ $J = 3{-}2/J = 2{-}1$ ratio, using a radiative transfer code (Pagani 2007, see Sect. 5.2). We derived values between 5×10^6 cm^{-3} and 10^7 cm^{-3}. Only IRAS 03282 shows a lower density (6×10^5 cm^{-3}). However, temperature and density decline with distance from the protostar, so lower spatial resolution observations trace lower average temperatures, densities, and (assuming spherical symmetry) lower column densities. Therefore, the N_2D^+ 3–2 lines trace, on average, warmer and denser gas than do the N_2D^+ 2–1 lines, and the densities obtained from the ratios are upper limits. For six sources, we also determined densities using the N_2D^+ $J = 2{-}1/J = 1{-}0$ ratios. We were not able to find a density that would reproduce all three lines simultaneously. The density values derived from the $J = 2{-}1/J = 1{-}0$ line ratio are about a factor 10 lower than those determined from the $J = 3{-}2/J = 2{-}1$ ratio. This difference again most likely arises because of the lower spatial resolution of the lower frequency observations.

4.2. Dust temperature

In general, T_{Dust} is expected to rise as a protostar evolves, but there is no exact model of dust temperature as a function of time. As a result, connecting dust temperature to specific protostellar ages depends on which model is used (see Froebrich 2005, and references therein).

All of our sources, with the exceptions of Per 4 S and SMM 5, have infrared counterparts identified in the IRAS point source or faint source catalogues. In addition, millimetre and submillimetre continuum data are available for many of the sources (see Table 6). We fitted these data to derive values for dust temperature (T_{Dust}) and emissivity (β) using Eq. (1) from Kramer et al. (2003):

$$F_\nu \propto \nu^{3+\beta} \cdot \frac{1}{e^{h\nu/kT_{Dust}} - 1}$$

where F_ν is the continuum flux at frequency ν. For 15 out of 16 sources for which more than two data points are available, a value of $\beta = 1$ yielded the best fit. Only for Barnard 5 IRS1 does an index of $\beta = 0$ (i.e. black-body radiation) yield a better result. In the three cases where data at only two frequencies were available, we assumed $\beta = 1$. This value is lower than the typical emissivity index of $\beta = 2$ for molecular clouds (e.g. Ward-Thompson et al. 2002; Visser et al. 1998). We propose that the lower emissivity indices found in the Class 0 sources are a result of strong temperature gradients and not inherent differences in the dust grains themselves. In fact, the cold envelopes are still bright at millimetre wavelengths, whereas practically all radiation emitted at $\lambda < 100\ \mu$m comes from the hot core. Therefore, the mass of dust radiating at longer wavelengths is much greater than the mass of dust radiating at shorter wavelengths, and the spectrum from the entire core gets flattened. We modelled the continuum emission using an emissivity index of two (see Sect. 5), but obtained as the index a β-value of one for the whole modelled cloud.

The dust temperatures derived from fitting the continuum data range from approximately 20 K up to 50 K (see Table 6). These temperatures are clearly higher than the excitation temperatures of N_2H^+ and the kinetic gas temperatures (Table 3). The difference is likely due to the dust emission from warmer regions being stronger than from cold dust, and thus the obtained average temperature is higher than the gas temperature traced by N_2H^+.

In Fig. 3, the N_2D^+/N_2H^+ column density ratio is plotted versus the dust temperature. All objects with N_2D^+/N_2H^+ ratio >0.15 have $T_{Dust} < 25$ K. At higher dust temperatures, the deuterium fractionation declines, reaching an average value of approximately 0.05 at 30 K.

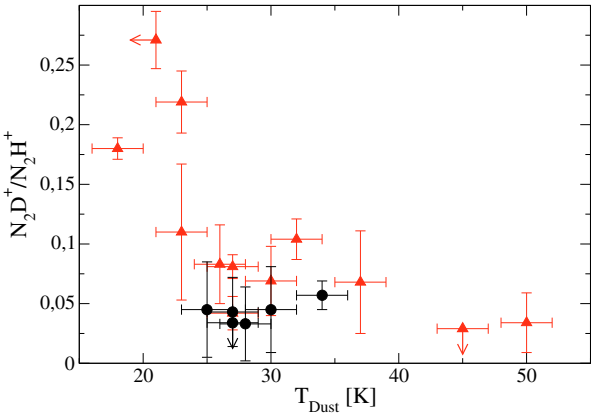

Fig. 3. Deuterium fractionation (N_2D^+/N_2H^+ column density ratio) versus dust temperature. The highest N_2D^+/N_2H^+ ratios are seen at the lowest temperatures. As T_{Dust} increases, the deuterium fractionation declines. The objects marked with triangles are located in the Perseus cloud.

4.3. CO freeze-out

Because CO is one of the main destroyers of H_3^+ and its deuterated isotopologues, the progenitors of N_2D^+, the N_2D^+/N_2H^+ ratio should be sensitive to CO depletion (e.g. Dalgarno & Lepp 1984; Roberts & Millar 2000). The CO depletion factor, f_D, is defined as

$$f_D = x_{can}/x_{obs}$$

where x_{can} is the canonical ISM abundance ratio of CO. In this work, $C^{18}O$ has been observed, so that $x_{can} = [C^{18}O]/[H_2] = 1.7 \times 10^{-7}$ (Frerking et al. 1982). The total number of hydrogen molecules within the beam is determined by the ~1 mm continuum emission (1.3 mm, 1.1 mm, or 850 μm), using the equation

$$\mathcal{N}_{H_2} = \frac{F_\nu \cdot d^2}{\kappa_\nu \cdot B_\nu(T_{Dust})} \cdot \frac{1}{\mu}$$

(Terebey et al. 1993), where F_ν is the continuum flux, d the distance to the object, $B_\nu(T_{Dust})$ the Planck function, T_{Dust} the dust temperature determined in the previous subsection, and μ the mass of an H_2 molecule. For the opacity per unit mass, κ_ν, we used a value of 0.005 cm^2/g at a wavelength of 1.2 mm (André et al. 1996). To calculate κ_ν at other wavelengths, we express the relation between opacity and wavelength as a power law

$$\kappa_\lambda = \kappa_0 \left(\frac{\lambda_0}{\lambda}\right)^\beta .$$

We used $\beta = 1$ (zero for Barnard 5 IRS1), as suggested by the fits to the continuum data (see Sect. 4.2). The values for κ make the strongest contributions to the uncertainties in the H_2 column densities. Some authors use values for κ twice as high as ours (e.g. Froebrich 2005).

To compare the ~ 1 mm continuum data with our $C^{18}O$ 1–0 observations, we have to estimate the continuum flux density within a 22″ beam. That the angular diameters of the protostellar envelopes are always greater than the beam is an important issue in this conversion. To compare data taken with different beam sizes, we follow the method of Terebey et al. (1993). They showed that the flux of a dark cloud with a density distribution $\rho = r^{-p}$ and a temperature distribution $T = r^{-q}$ can be described by

$$F_\nu \propto d^{1-(p+q)} \cdot \theta^{3-(p+q)}$$

where d is the distance and θ the beam size. In their sample of mostly Class 0 protostars, they determined 1.7 to be an appropriate value for $(p + q)$. We used this value to scale the flux from the continuum observations to the $C^{18}O$ beam size.

We determined the $C^{18}O$ column density by using the CTEX-method and by assuming that $C^{18}O$ emission is optically thin. Since the critical density of $C^{18}O$ is 60 times lower than that for N_2H^+, we expect that $T_{ex}(C^{18}O)$ will be higher than $T_{ex}(N_2H^+)$ and comparable to the kinetic gas temperature or even slightly higher, due to freeze-out of CO in the cold parts of the cloud. Since the beam sizes of the NH_3 observations that were used to derive T_{kin} vary between 40″ and 88″, we adopted a constant excitation temperature of 15 K for all sources. This assumption introduces some error (<15%) in the estimation of the depletion factor. The total number of $C^{18}O$ molecules is then calculated from

$$\mathcal{N}_{C^{18}O} = N_{C^{18}O} \cdot d^2 \cdot \Omega$$

where $\mathcal{N}_{C^{18}O}$ is the total number of $C^{18}O$ molecules within the beam, $N_{C^{18}O}$ is the $C^{18}O$ column density, d the distance to the protostar, and Ω the beam solid angle.

The derived depletion factors lie between 1 and 4 (Table 6). A value below 1 is found toward Barnard 5 IRS 1, and this may be an indication that the $C^{18}O$ canonical abundance is larger in this source. Indeed, the ^{13}CO abundances measured toward Barnard 5 by Pineda et al. (2008) are a factor of two larger than those measured by Frerking et al. (1982) toward Taurus. (The CO abundance variations of about a factor of 2 are well known in star-forming regions, e.g. Lacy et al. 1994.) However, given that CO abundance measurements are not individually available for all the sources, the $C^{18}O$ canonical abundance has been kept the same for the whole sample.

In the central panel of Fig. 4, we show the correlation between CO freeze-out and deuterium fractionation in our sample of protostars. In the top panel, we show the same correlation but for low-mass prestellar cores (Crapsi et al. 2005), and the correlation for massive prestellar cores in the bottom panel (Fontani et al. 2006). The correlation determined from our sample looks very similar to the correlation found for low-mass prestellar cores. For small depletion factors ($f_D(CO) < 3$), the deuterium fractionation is low as well (<0.1). For depletion factors greater than three, the N_2D^+/N_2H^+ ratio rises quickly until it reaches 0.25. The only difference between the protostellar and prestellar cores is that, in the prestellar cores, the deuterium fractionation stays low until the depletion factor is ~10. This behaviour reflects the fact that CO is highly depleted in the centre of prestellar cores, whereas it is not depleted in the centres of Class 0 sources. In high-mass prestellar cores, there is no dependence of the deuterium fractionation on $f_D(CO)$. Since the high-mass prestellar cores in the Fontani et al. (2006) sample are at greater distances (a few kpc), these observations might be affected by non-depleted, non-deuterated gas along the line of sight.

The sources that are *not* located in the Perseus cloud show lower deuterium fractionation than Perseus sources with the same CO depletion factor. One explanation for this difference is that the Perseus sources are embedded in a dense environment ($n_{H_2} \sim 10^4$ cm^{-3}, Kwon et al. 2006), whereas many of the other cores are isolated. Since CO is not expected to be frozen out in the embedding material, the CO depletion factors of the Perseus cores could be underestimated. However, systematic errors arising from the different spatial resolutions and different wavelengths of the continuum observations cannot be ruled out.

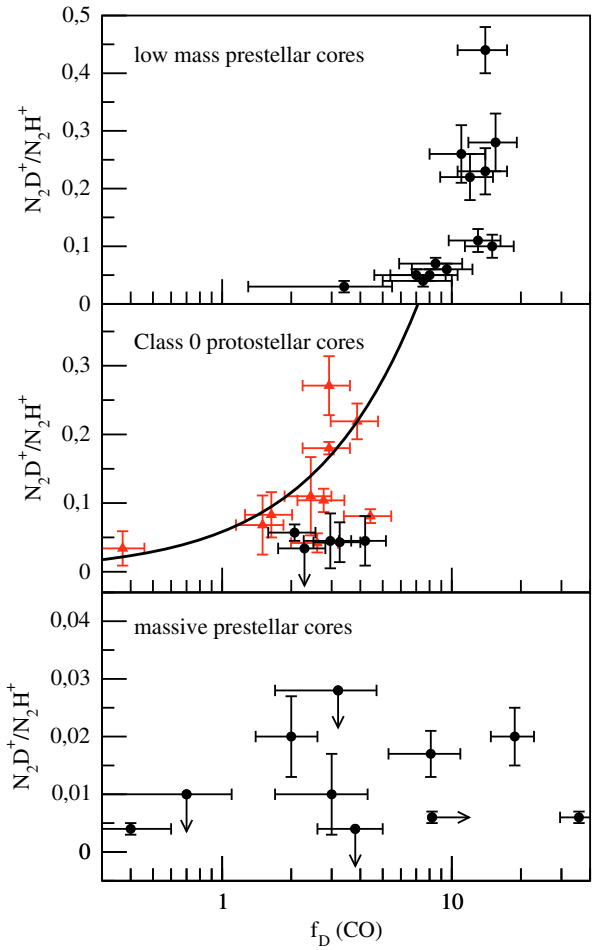

Fig. 4. N_2D^+/N_2H^+ column density ratio versus CO depletion factor for prestellar cores (*upper panel*, Crapsi et al. 2005), Class 0 protostars (*middle panel*, this work) and massive prestellar cores (*lower panel*, Fontani et al. 2006). The protostellar objects marked with triangles are located in the Perseus cloud. Among the Perseus objects, $f_D(CO)$ and the deuterium fraction appear correlated. The solid curve in the middle panel is the result of fitting the sub-sample of Perseus cores with a formula adopted from Caselli et al. (1998, see text).

The Perseus cores were observed at 1100 μm with a resolution of 31″ (Enoch 2006), and the other cores were observed at 1300 μm with a resolution of 40″ (Shirley et al. 2000). The Perseus source that does not appear to agree with the correlation is L 1448 IRS 3. It has a CO depletion factor of 4.4 but a low deuterium fractionation (0.081). This source is known to consist of multiple cores with several strong outflows (e.g. Volgenau et al. 2006; Looney et al. 2000), but it is not clear how this activity can decrease the deuterium fractionation while maintaining a large amount of CO freeze-out.

The correlation among the subsample of Perseus sources is quite good, whereas the non-Perseus sources do not show this functional dependence. We made a least-squares fit of the Perseus data to the equation

$$N_2D^+/N_2H^+ = \frac{c_1}{(c_2 + k_{CO} \cdot x_{can}(CO)/f_D(CO))},$$

which we adopted from expression (1) in Caselli et al. (1998). In this equation, $c_1 = 1/3 \cdot k_f \cdot x(HD)$, (where k_f is the formation rate of H_2D^+ and $x(HD)$ is the HD abundance), c_2 is the electron abundance ($x(e)$) times the dissociative recombination rate of H_2D^+, k_{co} is the destruction rate of H_2D^+ by CO, and $x_{can}(CO)$ the canonical CO abundance. The equation neglects the effect of multi-deuterated species and also assumes that dissociative recombination is a significantly faster process than recombination onto dust grains. A more comprehensive chemical model will be used in Sect. 5. The result of the least-squares fit is indicated in Fig. 4. The correlation coefficient is 0.71, indicating that the data agree fairly well with the expected theoretical fit. Using the reaction rates given by Caselli et al. (1998) and assuming a temperature of 10 K, we determined the HD abundance and the electron abundance. They derived an HD abundance of 3×10^{-5} is, as expected, quite close to the cosmic D/H ratio. The electron abundance we find is $\sim 7 \times 10^{-9}$, which is at the low end of the values found in dense cloud cores. However, due to the uncertainties in the temperatures, densities, and the determination of $f_D(CO)$ (see below), errors in the HD and electron abundances determined in this way may be as much as an order of magnitude.

The errors in the depletion factor are around 20 %. These errors do not include the uncertainties in the excitation temperatures, dust temperatures and κ's, which are the main sources of systematic errors in this analysis. A different κ value, however, would just rescale f_D, but it would not change the correlation itself. Such a rescaling would also be the effect of a different dust temperature, because $f_D(CO)$ was determined from continuum measurements around 1 mm, which is a wavelength clearly in the Rayleigh-Jeans regime. Rejecting the assumption of a constant average excitation temperature in all objects would change the correlation significantly.

If $T_{ex}(C^{18}O)$ is lower than 15 K, we *under*estimate the depletion factor, and we *over*estimate it if $T_{ex}(C^{18}O)$ is greater than 15 K. But, if we assume that $T_{ex}(C^{18}O)$ is related to the dust temperature, i.e. objects with higher T_{Dust} also have higher $C^{18}O$ excitation temperatures. Taking the correlation between the N_2D^+/N_2H^+ ratio found in the previous section into account, the high deuterium fractionation cores would may have higher $f_D(CO)$ values, and the low deuterium fractionation cores would have lower ones. Therefore the correlation would spread out fuorther along the depletion factor axis.

4.4. Bolometric luminosity

The SED of a young stellar object changes as the central protostar heats up the surrounding gas and dust. Several measures have been developed to determine how far a protostar has evolved, including the bolometric temperature (Myers & Ladd 1993), the ratio of the submillimetre to bolometric luminosity (André et al. 1993), and the correlation between luminosity (L) and visual extinction (A_v) (Adams 1990). Another measure of the evolution of a protostar, developed by Saraceno et al. (1996), is the ratio of L_{BOL} to $F_{1.3}^{D_0}$, the distance-normalised flux at 1.3 mm. As the protostar warms up, L_{BOL} should rise quickly, whereas $F_{1.3}^{D_0}$, which is a measure of the envelope mass and less dependent on the temperature, should stay constant or decrease slightly. Hence, the ratio $L_{BOL}/F_{1.3}^{D_0}$ increases as the protostar evolves.

To determine $F_{1.3}^{D_0}$ values, we use fluxes at $\lambda = 1.3$ mm (5 sources), 1.1 mm (4 sources), and 850 μm (2 sources). The continuum fluxes at 1.1 mm and 850 μm were corrected using, as before, $\beta = 1$ (or, in the case of Barnard 5 IRS 1, $\beta = 0$). For the distance normalisation and the conversion of the different beam sizes, we used the equation from Terebey et al. (1993) described in the previous section, i.e.,

$$F_{1.3}^{220\ pc} = F_{1.3}^{obs.} \cdot (d/220\ pc)^{0.7} \cdot (\theta/31'')^{-1.3},$$

Table 7. Bolometric luminosity and distance-normalised flux of Class 0 protostars in our sample.

Source	L_{BOL} [$L_\odot$]	$F_{1.3}^{220\ pc}$	$L_{BOL}/F_{1.3}^{220\ pc}$
L 1448 IRS 2	6.0[1]	0.80	7.5
L 1448 C	8.3[1]	0.53	15.6
L 1455 A1	9.7[1]	0.19	50.2
IRAS 03282	1.2[2]	0.32	3.8
Barnard 1-B	2.8	0.74	3.8
HH 211	3.6[1]	0.61	5.9
L 1527	1.9[1]	0.38	5.0
L 483	13.0[2]	0.70	18.5
SMM 5	3.6[1]	–	–
L 723	3.3[2]	0.45	7.4
B 335	3.1[2]	0.45	6.9
L 1157	5.8[2]	0.68	8.6

[1] Froebrich (2005); [2] Shirley et al. (2000).

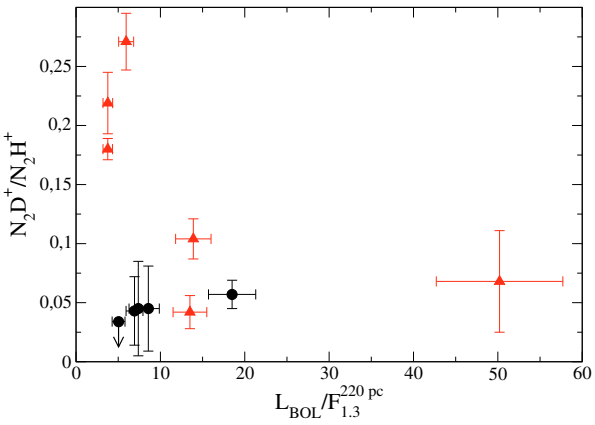

Fig. 5. N_2D^+/N_2H^+ versus $L_{BOL}/F_{1.3}^{D_0}$. All objects with high deuterium fractionation have low $L_{BOL}/F_{1.3}^{D_0}$ ratios and are likely to be young objects. L 1527, which has one of the lowest $L_{BOL}/F_{1.3}^{D_0}$ ratios, also has a quite upper limit on the N_2D^+/N_2H^+ ratio.

where $F_{1.3}^{obs.}$ is the continuum flux, d is the distance to the object, and θ is the beam size. We normalised all observations to a distance of 220 pc and a beam size (*FWHM*) of 31″. From the errors given for the continuum fluxes and bolometric temperatures, we estimate an error of 30% in the calculated $L_{BOL}/F_{1.3}^{D_0}$ ratios. The resulting normalised fluxes and the bolometric luminosities for the cores are listed in Table 7.

The correlation between $L_{BOL}/F_{1.3}^{D_0}$ and N_2D^+/N_2H^+ is shown in Fig. 5. The objects with the highest deuterium fractionation (>0.15) (IRAS 03282, Barnard 1-B and HH 211) all have low $L_{BOL}/F_{1.3}^{D_0}$ ratios and are presumably less-evolved protostars. As the $L_{BOL}/F_{1.3}^{D_0}$ ratio increases, the deuterium fractionation drops quickly. If one considers just the Perseus cores, then the fall-off of the deuterium fractionation is less steep. The $L_{BOL}/F_{1.3}^{D_0}$ ratios may be lower in the non-Perseus sources because systematic errors in normalisation (see Sect. 4.3) lead to overestimates of the continuum fluxes. L 1455 A1 has by far the highest $L_{BOL}/F_{1.3}^{D_0}$ ratio, and by this measure should be the most evolved protostar in the figure. The assertion that L1455 A1 is more evolved than other protostars is reinforced by the relatively low CO depletion factor and high dust temperature. L 1527 is a notable outlier in the sample. Its $L_{BOL}/F_{1.3}^{D_0}$ ratio is one of the lowest in our sample (5.0), but it has an N_2D^+/N_2H^+ ratio <0.034 (more discussion on this source is presented in 4.7).

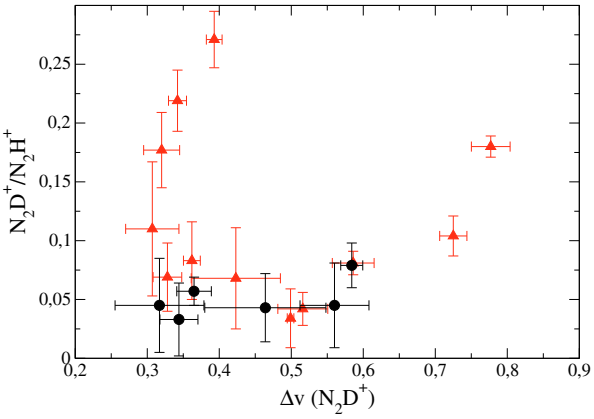

Fig. 6. *FWHM* of N_2D^+ 2-1 versus N_2D^+/N_2H^+. Triangles are Perseus cores.

4.5. Kinematic of the gas

So far, we have correlated the N_2D^+/N_2H^+ ratios with physical parameters, which are all related to temperature, and thus to the evolutionary stage of the protostar. In this section, we investigate the relation of deuterium fractionation to parameters linked to the kinematics of the gas. Infall, for example, heats up the gas and is expected to influence the gas-phase chemistry.

First, we compare the N_2D^+/N_2H^+ ratios with the N_2D^+ 2−1 line widths (Table 3). Processes such as thermal broadening, turbulent motions, and systematic motions, e.g. infall, all contribute to the full width at half maximum (*FWHM*) of optically thin emission lines. Thermal broadening plays a relatively minor role, since the thermal line width (*FWHM*) of N_2D^+ at 10 K is only 0.12 km s^{-1} (0.17 km s^{-1} at 20 K).

In Fig. 6, the N_2D^+/N_2H^+ column density ratio is plotted versus the *FWHM* of N_2D^+ (2−1). Most of the protostars with high N_2D^+/N_2H^+ ratios have narrow N_2D^+ lines. The two exceptions are Barnard 1-B (Δv = 0.78 km s^{-1}) and L 1448 C (Δv = 0.72 km s^{-1}), which show the broadest N_2D^+ lines in the sample. However, all Perseus sources with $\Delta v > 0.5$ km s^{-1}, including Barnard 1-B and L 1448 C, have multiple embedded sources (Volgenau 2004; Matthews & Wilson 2002). The relative velocity differences between the individual protostars leads to additional line broadening.

To be able to trace only the systematic motion of the gas, e.g. infall motion, we used the asymmetry parameter δv, which was defined by Mardones et al. (1997) as

$$\delta v = \frac{v_{thick} - v_{thin}}{\Delta v_{thin}},$$

where v_{thick} is the velocity of an optically thick line, v_{thin} the velocity of an optically thin line, and Δv_{thin} its line width. As shown by Mardones et al., infall yields a negative value for δv. If infall dominates the kinematics of the protostar, then an absorbing foreground component will appear redshifted with respect to the core, causing an optically thick line to appear blueshifted. We used HCO^+ 3−2 as the optically thick line and N_2H^+ 1−0 as the optically thin line. The velocity of the optically thin N_2H^+ line is derived using the HFS method of CLASS (see Sect. 3). We also compare the resulting velocities with those derived by fitting a single Gaussian to the isolated $1_{01} \rightarrow 1_{12}$ component, following Mardones et al. The velocities calculated with the two different methods are not always coincident, but the differences are within the velocity resolution of 0.06 km s^{-1}. Because a fit to seven lines has a lower error than a fit to only one hyperfine component, we

Table 8. Velocities of $C^{18}O$ and HCO^+ lines and asymmetry parameters.

Source	v [km s^{-1}] N_2H^+	v [km s^{-1}] HCO^+	δv	R/B
L 1448 IRS 2	4.12	4.53	0.82*	1.28
L 1448 IRS 3	4.62	5.40	0.84	–
L 1448 C	4.95	5.45	0.66	2.21
L 1455 A1	5.10	5.12	0.03	–
L 1455 A2	4.88	4.94	0.17	–
Per 4 S	7.52	7.25	–0.92	–
Per 4 N	7.57	7.44	–0.40	–
Per 5	8.15	7.65	–1.31	–
Per 6	5.94	6.02	0.05	1.82
IRAS 03282	6.06	6.62	–0.91	0.57
Barnard 1-B	6.62	6.01	–0.74	0.45
HH 211	9.12	9.27	0.37*	1.47
Barnard 5 IRS 1	10.27	10.29	0.05	3.88
L 1527	5.90	5.38	–1.60	–
L 483	5.40	5.87	1.06	3.18
SMM 5	8.12	8.18	–0.33	–
L 723	11.11	11.43	0.46	1.61
L 673 A	6.87	6.97	0.19	–
B 335	8.34	7.90	–1.10*	0.833
L 1157	2.67	3.16	0.75	1.54

Values for δv marked with * are ambiguous due to nearly equal peak intensities of the double-peaked HCO^+ line, i.e. the R/B ratio is close to one.

use in the following the v_{LSR} obtained by the HFS method. For v_{thick}, we use the peak velocity of the HCO^+ 3–2 line. In cases where the HCO^+ lines are double-peaked, we follow Mardones et al. (1997) and use the velocities of the stronger of the two peaks (although in some spectra the stronger peak was ambiguous). An alternative asymmetry parameter is the ratio of the red peak intensity to the blue peak intensity (R/B) of optically thick, double peaked lines. In such cases, $R/B < 1$ indicates infall. Since more than 50% of the observed HCO^+ lines show double-peaked line shapes, we also calculate these ratios. The results for both asymmetry parameters are listed in Table 8.

In our sample, we find eight sources with a clear indication of infall (i.e. $\delta v < -0.25$) and seven sources with redshifted, optically thick lines (i.e. $\delta v > 0.25$). For five sources, there is no clear indication of systematic motion ($-0.25 < \delta v < 0.25$). Like previous studies by Mardones et al. (1997) and Gregersen et al. (2000), we find more blueshifted than redshifted objects. The blue excess is defined by Mardones et al. (1997) as

$$\text{blue excess} = \frac{N_{\text{blue}} - N_{\text{red}}}{N_{\text{total}}}$$

where N_{blue} is the number of objects with $\delta v < -0.25$ and N_{red} is the number of objects with $\delta v > 0.25$. In our sample, the blue excess is 0.05 ± 0.2. If we exclude the objects with an ambiguous δv due to nearly equal peak intensities of the double peaked HCO^+ line, we derive a blue excess of 0.12 ± 0.2. Both values are slightly lower, but still agree within the errors with 0.28 and 0.25, the values found by Gregersen et al. (2000) and Mardones et al. (1997), respectively.

δv and, less clearly, R/B are correlated with the deuterium fractionation, and only Per 5 and, once again L 1527, which is a peculiar source (see Sect. 4.7), do not follow the general trend and indicate strong infall motion. The higher the N_2D^+/N_2H^+ ratio, the more blueshifted the optically thick emission lines. Such a result was somehow expected, since outflow activity rises with the evolution of the protostar (Richer et al. 2000). The results are also in good agreement with the results of

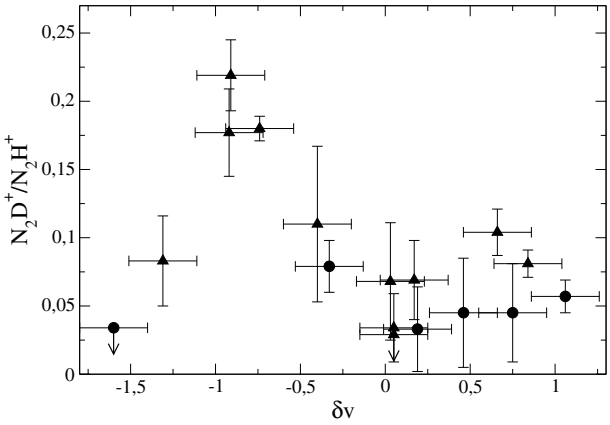

Fig. 7. Asymmetry parameter δv versus N_2D^+/N_2H^+ ratio. Only the sources with an unambiguously determined asymmetry parameter are shown. All sources with enhanced deuterium fractionation are located at moderate δv of about −0.4, and is increasing with decreasing deuterium fractionation.

Mardones et al. (1997). Using observations of CS, $C^{34}S$ and H_2CO lines, they found that the blue excess of Class 0 protostars is clearly enhanced compared to Class I objects. However, using observations of HCO^+, $H^{13}CO^+$ and N_2H^+ lines, Gregersen et al. (2000) did not find such trend. They speculate that infall asymmetry disappears later in HCO^+. Because our sample contains no true Class I objects, we cannot directly compare their results with ours.

We also calculated δv using the $C^{18}O$ 1–0 transition as the optically thin line. Contrary to N_2H^+, which traces the cold, CO depleted envelope, $C^{18}O$ traces the already warmed up central part of the protostar. Thus it traces the region, where the HCO^+ 3–2 line comes from, too. But due to the lower critical density of the $C^{18}O$ 1–0 transition, the low-density outskirts of the protostellar envelope might contribute significantly to the $C^{18}O$ emission, which possibly dilute any correlation. Qualitatively, the correlation between δv and the deuterium fractionation looks similar, no matter which optically thin line is used. However, for objects with an N_2D^+/N_2H^+ ratio above 0.75, δv determined with $C^{18}O$ yields less blue-shifted values. A reason for this difference might be that in these objects, which also show the highest CO depletion factors, the contributions from the environmental material to the $C^{18}O$ emission is expected to be biggest. The bigger contribution of the environmental material is also indicated by the fact that for objects with $\delta v_{N_2H^+}$ lower than −0.5, $\Delta v(C^{18}O)$ is on average 2.4 times larger than $\Delta v(N_2H^+)$, whereas for the remaining sources $\Delta v(C^{18}O)$ is only 1.6 times larger. More turbulent material appears to surround infalling protostellar envelopes.

4.6. Comparison of the deuterium fractionation of different molecules

The deuterium fractionation of N_2H^+ reflects the present time temperature and density better than most other molecules, since it does not significantly deplete (see e.g. Caselli et al. 2002b; Bergin et al. 2002; Schnee et al. 2007), and the chemical reactions for N_2D^+ formation and destruction are quite fast and simple. Memories of cold phases in the past of the dark cloud core are therefore not expected in the observed N_2D^+/N_2H^+ ratio. In this section, we compare the N_2D^+/N_2H^+ ratio with the NH_2D/NH_3 (Hatchell 2003), DCO^+/HCO^+ ratios (Jørgensen et al. 2004) and the deuterium fractionation of H_2CO and

Table 9. Deuterium fractionation of several molecular species.

Source	$\frac{N_2D^+}{N_2H^+}$ [1]	$\frac{NH_2D}{NH_3}$ [2]	$\frac{DCO^+}{HCO^+}$ [3]	$\frac{D_2CO}{H_2CO}$ [4]
L1448 IRS 3	0.081	0.17	–	–
L1448 C	0.104	0.20	0.011	0.24
IRAS 03282	0.219	0.22	–	–
HH 211	0.271	0.33	–	–
Barnard 5	0.034	0.18	–	–
L 1527	< 0.034	–	0.048	0.44
L 483	0.057	–	0.006	–
L 723	0.045	–	0.004	–
L 1157	0.045	–	0.016	≤0.08

[1] This work; [2] Hatchell (2003); [3] Jørgensen et al. (2004); [4] Parise et al. (2006).

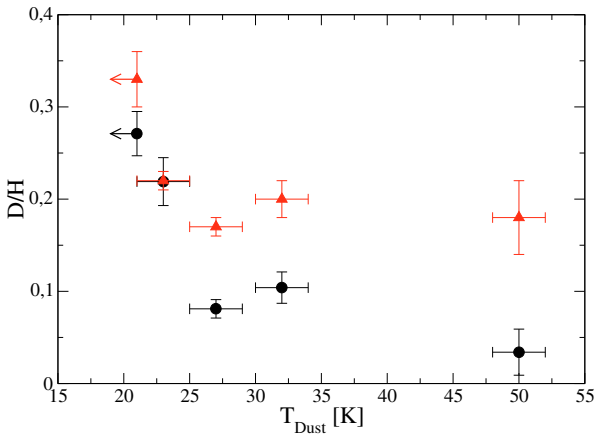

Fig. 8. Deuterium fractionation of NH_3 (red triangles) and N_2H^+ (black circles) versus dust temperature.

CH_3OH (Parise et al. 2006) for the sources in our sample where these data are available (Table 9).

The deuterium fractionation of HCO^+ is significantly lower than the fractionation of N_2H^+ in all objects but one (L 1527). This difference can be explained by CO, the parent species of HCO^+, also being the main destroyer of H_2D^+ and thus the DCO^+/HCO^+ ratio traces only those regions where the deuterium fractionation in N_2H^+ is expected to be lower. Furthermore, Jørgensen et al. (2004) determine the DCO^+/HCO^+ ratio using the DCO^+ $J = 3–2$ line, which has a critical density of 1.4×10^6 cm^{-3}. Therefore these DCO^+ observations mostly trace the inner, high density part, which might already be warmed up by the embedded protostellar core, thus lowering the DCO^+/HCO^+ ratio. The situation with NH_3 is different. Like N_2H^+, NH_3 is formed from N_2 and does not seem to freeze out (Tafalla et al. 2002). Thus, N_2D^+ and NH_2D emission should originate from the same region. As a consequence, the deuterium fractionation of N_2H^+ and NH_3 should be comparable.

As shown in Fig. 8, the coldest objects, i.e. the youngest objects in our sample (HH 211 & IRAS 03282), have a deuterium fractionation of NH_3 indeed comparable to the fractionation of N_2H^+. But the warmer the dust gets, the more the ratios diverge. The NH_2D/NH_3 ratio is about 0.2 at T_{Dust} = 50 K, where the N_2D^+/N_2H^+ ratio is five times lower. The differing trends in the two ratios can be explained as follows. Both N_2D^+ and NH_2D are formed directly or indirectly via H_2D^+ or its multiply deuterated forms, i.e., the formation mechanism is only effective in cold, CO-depleted environments. In regions where CO desorbs from the dust due to the warming up of the protostar, N_2D^+ and N_2H^+ disappear quickly from the gas phase, because these species are directly destroyed by CO, forming HCO^+ and DCO^+, respectively. Thus, with increasing temperature, the N_2D^+/N_2H^+ ratio traces material at larger and lager radii (i.e. at lower and lower densities). But deuterium fractionation is related to the density, because of the lower degree of CO depletion at lower densities (see Sect. 5.4 and Fig. 11). In contrast to N_2H^+ and N_2D^+, which are pure gas-phase species, ammonia is also found on dust grain mantles, most likely formed by grain-surface reactions (Boogert et al. 2008). The solid NH_3, which desorbs from the dust grains as soon as the environmental material warms up, likely has a large deuterium fractionation due to the fossil record of grain surface chemistry and gas phase depletion at low temperatures (e.g. Aikawa et al. 2008). Thus, the observed NH_2D/NH_3 ratio declines more slowly than the deuterium fractionation of pure gas phase species.

Deuterated formaldehyde (HDCO and D_2CO) are very abundant, too. The $HDCO/H_2CO$ ratio, as well as the D_2CO/H_2CO ratio, are close to 0.1 (Parise et al. 2006). In their work, Parise et al. also determined the deuterium fractionation of methanol, which even exceeds the deuterium fractionation of formaldehyde (e.g. $CH_2DOH/CH_3OH \sim 0.5$). For both molecules, no obvious correlation between the deuterium fractionation and the core evolutionary stage could be found. Because mainly grain surface chemistry is involved in the deuteration of methanol and formaldehyde, the observed deuterium fractionation is probably a memory of the previous, prestellar phase (Ceccarelli et al. 2001), a similar (although more extreme) case to the one found for ammonia.

4.7. Evolutionary sequence of the sample

The youngest objects in our sample are Barnard 1-B, IRAS 03282 and HH 211. All three evolutionary tracers indicate those sources are among the youngest. The depletion factor, f_D(CO), indicates that L1448 IRS3 and L 1157 are young objects, too, but their T_{DUST} suggest that these sources are, instead, more evolved. A possible solution to this discrepancy lies in acknowledging several assumptions we made in determining the CO depletion factor (e.g. in converting the beam sizes of the continuum and the $C^{18}O$ observations). Although, overall, these assumptions seem to be justified, they might not be valid for all sources, and thus the f_D (CO) values may be less accurate. The three protostars we identified as the youngest also have the highest N_2D^+/N_2H^+ ratios (0.18, 0.22, and 0.27 in Barnard 1-B, IRAS 03282, and HH 211, respectively). By this measure, Per 4 S, with a deuterium fractionation of 0.177, should also be very young, but no complementary data are available to confirm this.

The objects at a moderate evolutionary stage are those with a deuterium fractionation around 0.1 (L 1448 IRS 3, PER 4 N, PER 5). The exception is L 1448 C ($N_2D^+/N_2H^+ = 0.10$), which seems to be more evolved than the others. However, among these intermediately-evolved sources, there are also some with deuterium fractionations of ~0.05 (L 723, B 335, L 1448 IRS 2). For SMM 5 ($N_2D^+/N_2H^+ = 0.079$), we are unable to determine the evolutionary stage independently, but, because of its N_2D^+/N_2H^+ ratio, we think that it belongs to the group of intermediately-evolved objects. The N_2D^+/N_2H^+ ratios of the most evolved protostars are, with the exception of L 1448 C (0.10), ~0.05.

L 1527 is a special case. The T_{Dust} (27 K) and especially the $L_{BOL}/F_{1.3}^{D_0}$ ratio (5.0) suggest that it is a younger object, but its low N_2D^+/N_2H^+ ratio and the fact that an embedded source is detected at wavelengths <5 μm indicates that this source is more evolved (Froebrich 2005). Chemical models, which reproduce the observed abundance of long-chain unsaturated hydrocarbons and cyanopolyynes, indicate a more evolved evolutionary stage of L 1527 as well (Hassel et a. 2008). From infrared observations, Tobin et al. (2008) conclude that L 1527 contains a massive protostellar disc, which is seen edge-on. Therefore L 1527 might be a more evolved object than indicated by continuum observations, due to the large obscuration of the central object. Hence, the N_2D^+/N_2H^+ ratio seems to be even more reliable than continuum measurements at identifying the youngest protostellar objects.

In conclusion, the N_2D^+/N_2H^+ ratio can be used to clearly identify the youngest objects among the Class 0 sources. For more evolved objects, the correlation of evolutionary stage and N_2D^+/N_2H^+ ratio is not so clear, but an overall decrease in deuteration with evolutionary stage can be seen.

5. Comparison with chemical- and radiative transfer models

To explain the results discussed in the previous section, we examined a model of a "typical" Class 0 object rather than a specific source. First, we describe the physical properties, e.g. the temperature and density profiles, of the model. Subsequently, we calculate the abundances of the important species and apply a radiative transfer code to simulate the observations.

5.1. Cloud structure

The density structure of the model is that of a singular isothermal sphere (Shu 1977):

$$n(r) \propto r^{-2}.$$

Such density profiles have been found for Class 0 protostars, too (Lonney et al. 2003). The inner boundary of the protostellar envelope is set to 100 AU. This limit is arbitrarily chosen, but at a distance of 220 pc, which is the distance of the Perseus molecular cloud, 100 AU corresponds to an angle of 0.46″, which is much smaller than the angular resolution of our observations. Therefore, the model results are not sensitive to the chosen inner boundary. The outer boundary is defined by the radius where the density is 10^4 cm^{-3}. Kirk et al. (2006) estimate the external pressure on cores in the Perseus region and find values of $\log_{10}(P_{ext}/k)$ between 5.5 and 6.0. Assuming a temperature between 15 and 30 K, this leads to a gas density between $\sim 10^4$ cm^{-3} and $\sim 5 \times 10^4$ cm^{-3}. Around L 1448 IRS 3, Kwon et al. (2006) find a density of $6–9 \times 10^3$ cm^{-3}. Thus, 10^4 cm^{-3} can be considered an average value for the gas number density surrounding Perseus cores.

The total envelope mass is assumed to be close to a few solar masses. However, since the model results depend strongly on the density, the total mass varies for different models (see below). For the temperature profile, we use a power law with an index of −0.4, which is the exponent for optically thin emission from protostellar envelopes, as found by Looney et al. (2003). They also show that, with a density powerlaw index of 2, the radial temperature distribution can significantly deviate from the power-law at radii smaller than 100–200 AU. However, given that we used an inner boundary of 100 AU for the envelope, such deviations do not noticeably influence our model. To avoid very low temperatures on the outskirts of the envelope, we assume a temperature profile like the one found in prestellar cores (Crapsi et al. 2007):

$$T(r) = T_{out} - \frac{T_{out} - T_{in}}{1 + (r/r_0)^{1.5}}.$$

Here, we assume T_{out} = 15 K, T_{in} = 7 K, and r_0 = 3633 AU. This radius corresponds to an angle of 26″ at a distance of 220 pc, as found in L 1544. However, since we use this temperature profile only for the outer, low-density part of the envelope, the influence of these parameters on the model results is negligible. Density and temperature profiles are shown in Fig. 9.

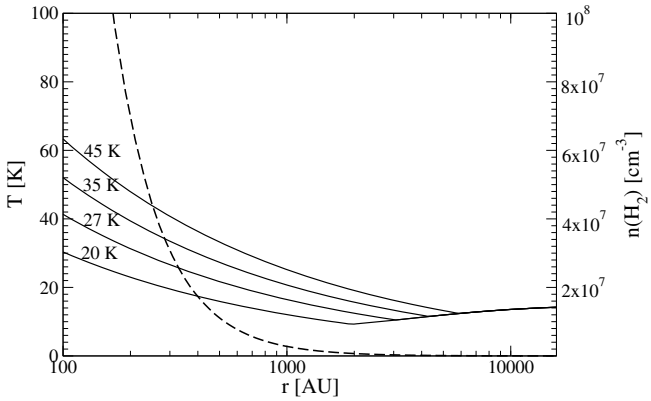

Fig. 9. Density (dashed line) and temperature (solid lines) profiles of the protostellar core models. The four temperature profiles represent models that yield values for T_{Dust} of 20 K, 27 K, 35 K, and 45 K.

Using this cloud structure, we calculate the continuum flux at 60 μm, 100 μm, 850 μm, and 1.2 mm from the formula:

$$F_\nu = \int n(r) \cdot B_\nu(T(r)) \cdot \kappa_\nu \cdot \mu \, dr$$

where n is the density, $B(T)$ the Planck function, and μ the mass of the gas molecules. For the opacity per unit mass, κ_ν, we again use 0.005 g/cm^2 at 1.2 mm, which assumes optically thin continuum emission. Furthermore, we assume an emissivity index of β = 2, which is a typical value for molecular clouds (Ward-Thompson et al. 2002) and not the β = 1 shown by previous fits. We use β = 2, because the cold (~10 K) outskirts of the envelope still emit a significant amount of radiation at mm wavelengths, but much less at 60 μm. The strong temperature gradient in protostellar cores causes the spectrum integrated over the entire core to be flattened. Thus, the emissivity index derived from a single temperature fit is underestimated. The values for the continuum emission obtained by this method are then fitted, following the procedure described in Sect. 4.2, and the absolute temperature scale is varied to obtain models with dust temperatures of 20 K, 27 K, 35 K, and 45 K, which covers the whole range of observed values.

5.2. Chemical and radiative transfer model

The chemical code used in this study is similar to the one originally described by Caselli et al. (2002b), but updated following Caselli et al. (2008). We assume a spherically symmetric cloud, and follow the time-dependent freeze-out of CO and N_2, as well as thermal and non-thermal desorption due to cosmic-ray impulsive heating, neglecting dynamical effects. All the deuterated forms of H_3^+ are included in the model, and the abundances

of the ionic species, such as HCO^+, N_2H^+, and their deuterated couterparts, are given by the steady-state chemical equations using the instantaneous abundaces of the neutral species (see Caselli et al. 2002b, for details). The rate coefficients are adopted from the UMIST database for astrochemistry, available at http://www.udfa.net. For the proton-deuteron exchange reaction (such as $H_3^+ + HD \rightarrow H_2D^+ + H_2$), we use both "standard rates" (e.g. as used in Roberts et al. 2004; Ceccarelli & Dominik 2005) as well as the rates more recently measured by Gerlich et al. (2002), which appear to better fit our data (see below). No atomic oxygen is included in the code, given the large uncertainties in its abundance in cold and dense regions (e.g. Bergin & Snell 2002; see also discussion in Sect. 3.2.3 of Caselli et al. 2002b). The cosmic-ray ionization rate is fixed at $\zeta = 3 \times 10^{-17}$ s^{-1}, the average value measured toward high-mass star forming regions by van der Tak & van Dishoeck (2000). The CO and N_2 binding energies are assumed to be 1100 K and 982.3 K, respectively, following the prescriptions of Öberg et al. (2005) and Schnee et al. (2007) (see their Sect. 6.2). The model is run for 10^6 yr, an average age for a dense core. After 10^6 years, the abundances of the various molecules nearly reache chemical equilibrium, and thus the exact evolution time is not a critical parameter (see Sect. 5.5 for discussion).

The results from the chemical model are used as input parameters for a radiative transfer model, a non-LTE Monte-Carlo code developed by Pagani et al. (2007). This code, which is developed from the Bernes code (Bernes 1979), calculates the 1D radiative transfer of both N_2H^+ and N_2D^+ and includes line overlap of the hyperfine transitions. Furthermore, recently published collisional coefficients between individual hyperfine levels have been implement (Daniel et al. 2005). For the convolution with the beam, we assumed a Gaussian beam shape with *HPBW* as listed in Table 2. The distance to the cloud is set to 220 pc, i.e. the distance of the Perseus cloud. From the spectra that we obtained from the Monte-Carlo-code, we determined the N_2D^+/N_2H^+ ratio using the CTEX procedure, just as we did for the observed spectra (see Sect. 4.1). Hence, the comparison between the model and the observations is consistent, because possible systematic errors, introduced by the assumption of a constant excitation temperature, are taken into account.

5.3. Comparison between models and observations

We computed the N_2D^+/N_2H^+ ratios for four models with fitted dust temperatures of 20 K, 27 K, 35 K and 45 K, respectively. The deuterium fractionation in these models ranges from 0.23 at 20 K to 0.03 at 45 K. These values fit the observations very well. We derived an H_2 density at a radius of 100 AU of 2.77×10^8 cm^{-3}, which corresponds to a total envelope mass of 4.6 $M_\odot$. The modelled correlation between the deuterium fractionation and the CO depletion factor (f_D (CO)) fits the observations quite well, too, but in the cooler objects ($T_{Dust} \sim 20$ K), the modelled CO freeze-out is very sensitive to the temperature. Thus, a marginal temperature variation leads to a significant change of the CO depletion factor, and therefore the quality of the fit depends strongly on the model used. In Fig. 10, a comparison of the models with the observations of the Perseus sources is shown. Results from the models are also listed in Table 10. The best agreement with observations is found when using the reaction rates measured by Gerlich et al. (2002) for the proton-deuteron exchange reaction. Using the "standard rates", we could only fit the observed N_2D^+/N_2H^+ ratios by increasing the total envelope mass to 25 $M_\odot$, a value that is clearly higher than expected for low-mass protostars.

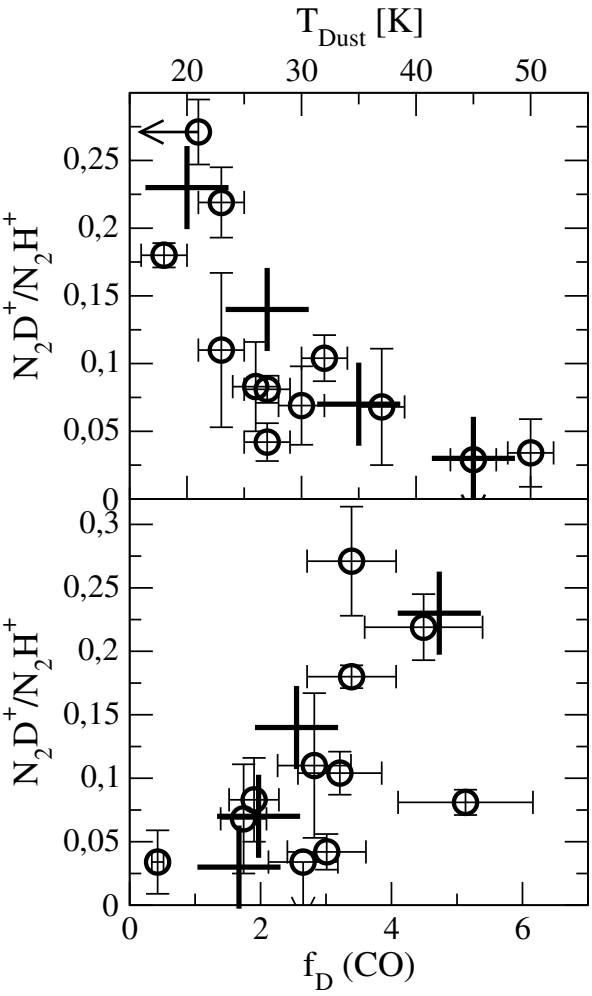

Fig. 10. *Upper panel*: N_2D^+/N_2H^+ ratio versus dust temperature. *Lower panel*: N_2D^+/N_2H^+ ratio and the CO depletion factor F_D (CO). The open circles are the observed values for the subsample of cores in the Perseus cloud; the crosses are the model results. The N_2D^+/N_2H^+ ratio of the models was determined using the CTEX method.

Table 10. Model results.

T_{Dust}	N_2D^+/N_2H^+ (CTEX)	HCO^+/DCO^+	f_D(CO)
20 K	0.23	0.09	4.73
27 K	0.14	0.05	2.55
35 K	0.07	0.03	1.97
45 K	0.03	0.02	1.67

To check that the assumption of a constant excitation temperature does not give a significantly different result from the $T^{-0.4}$ profile, we calculated beam-averaged column densities from the model abundance profiles as well. The N_2D^+/N_2H^+ ratios determined from the beam-averaged column densities are the same as before, to within 20%. The estimated error of the observed N_2D^+/N_2H^+ ratio is also approximately 20%, so the fit is good, independently of the method used. The trend of a decreasing deuterium fraction with increasing T_{Dust} is true for both the ratio determined by the CTEX method and the ratio of the beam-averaged column density.

The N_2D^+ $J = 3–2/J = 2–1$ intensity ratios of the models range from 0.44 to 1.10, which is comparable to the observed ratios. For the $J = 2–1/J = 1–0$ ratios, the models give values that are a factor of two higher than what is observed. However, these

ratios are very sensitive to temperature, density, and abundance variations. Taking the simplicity of our model into account, we consider these values to agree with the observations.

Besides N_2D^+ and N_2H^+, the abundances of HCO^+ and DCO^+ were also calculated by the chemical model. The DCO^+/HCO^+ ratio is significantly lower than the N_2D^+/N_2H^+ ratio and ranges from 0.02 to 0.08 in the models with dust temperatures of 45 K and 21 K, respectively. The HCO^+ and DCO^+ column densities are averaged over a 21″ beam, and thus comparable to the observations conducted by Jørgensen et al. (2004). The values for the DCO^+/HCO^+ ratio reported by them are between 0.004 and 0.048 and thus a little lower than the modelled ratios (see Tables 10 and 9).

5.4. Chemical stratification within the core

The temperature gradient, caused by the heating of the central object, leads to strong variations in the abundances of many molecules and molecular ions. The more immediate cause of these variations is the freeze-out of CO, which occurs at a temperature of ~20 K. The absence of CO in the gas phase has a big influence on the abundance of many other species, since many molecular ions, e.g. N_2H^+, are partially destroyed by reactions with CO. In addition, the deuterium fractionation is enhanced in regions where CO is depleted (see Sect. 1). Therefore, the protostellar envelope can be roughly divided into three zones (Fig. 11). In the inner zone, the temperature has increased above ~20 K, CO evaporates from the grains and, consequently, the abundance of N_2H^+ as well as the deuterium fractionation, are relatively low in this region. As soon as the temperature drops below the critical value of ~20 K, the CO abundance drops drastically. At the same time, the N_2H^+ abundance rises by 1–2 orders of magnitude. The N_2D^+/N_2H^+ ratio rises as well, but its maximum is at a larger radius than the CO abundance minimum. This is because the temperature at the minimum of the CO abundance is ~20 K, where the destruction of H_2D^+ via the reaction $H_2D^+ + H_2 \rightarrow H_3^+ + HD$ is not neglible. At even larger radii, the degree of CO depletion decreases as the gas density decreases, which causes the N_2H^+ abundance to stay more or less constant, and the deuterium fractionation to drop again.

During the Class 0 phase, the temperature of the central object increases, as does the temperature of the envelope. Consequently, the radius at which CO freezes out onto dust grains shifts farther outwards, and the fraction of the cloud in which the abundance of deuterated molecules is enhanced gets smaller with time. Furthermore, the mean density of the deuterium fractionated gas decreases, thus the mean local N_2D^+/N_2H^+ ratio declines as well. This leads to the decrease in the N_2D^+/N_2H^+ column density ratio, which we observe in our sample.

The reason for the different ratios of the deuterated and non-deuterated forms of HCO^+ and N_2H^+ is that the deuterium fractionation is strongest in places where CO, a progenitor of HCO^+ and DCO^+, is mostly depleted. Thus, in contrast to N_2H^+, HCO^+ is also relatively strong in the warm and dense inner part of the envelope, and the ratio of the column densities of DCO^+ and HCO^+ is significantly lower than the N_2D^+/N_2H^+ ratio. This can be seen in Fig. 12, in which the abundance of the molecules and molecular ions are shown as a function of radius.

The radial abundance profiles we found with our static model are in good agreement with the results of Lee et al. (2005), who calculated a self-consistent dynamical and chemical model of the entire star forming process. In their model, the deuterated species are not calculated, but the abundance profiles of CO, N_2H^+ and HCO^+ at a time ~10^5 yr after the collapse starts are similar to the profiles we found (see their Fig. 11). This similarity indicates that the assumption of a chemical equilibrium is valid at least for the simple species. In a more recent paper, Aikawa et al. (2008) get somewhat shorter timescales for the protostellar evolution: 9.3×10^4 years after the beginning of the collapse, the CO desorption radius is ~2000 AU, which is comparable to the results of our 45 K model. But even for these

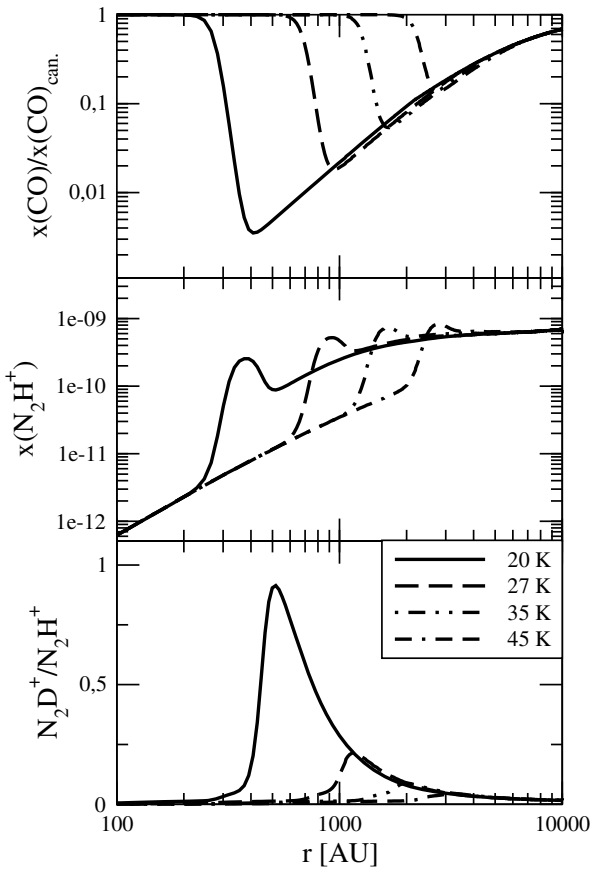

Fig. 11. The relative abundance of CO (*upper panel*), N_2H^+ (*middle panel*), and the N_2D^+/N_2H^+ ratio are shown as a function of radius. It can be clearly seen that the radius at which CO starts to deplete shifts outwards with increasing temperature, as does the peak of the deuterium fractionation.

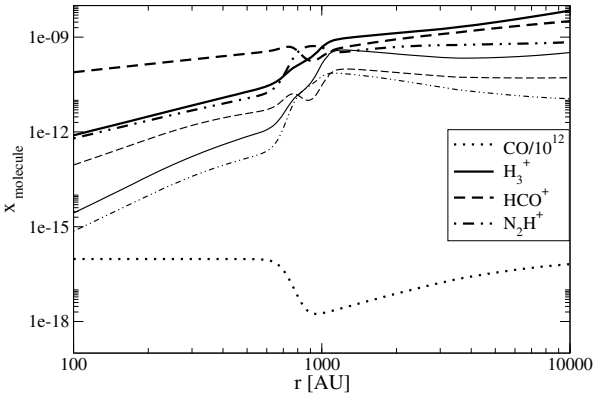

Fig. 12. The abundances of CO, H_3^+, H_2D^+, HCO^+, DCO^+, N_2H^+, and N_2D^+ relative to H_2 are shown as a function of radius. The thick lines show the abundance profile of the protonated species. The thin lines show their singly-deuterated counterparts. These profiles apply to the model with T_{Dust} = 27 K.

shorter time scales, the assumption of chemical equilibrium is still valid (see next section).

5.5. Sensitivity of the model

The evolution times of the models are the least constrained values. The estimated ages of Class 0 protostars range from $\sim 10^4$ to a few times 10^5 years after the collapse has started (Froebrich 2005). The ages vary by a factor of 10 depending on which model is used. However, the crucial time for the deuterium chemistry is the time since the CO started to freeze out, because the freeze-out of CO is the slowest reaction in the network. Thus, the entire prestellar phase has to be taken into account. After a time of 10^6 years, the abundances have already reached equilibrium. Reducing the time to 10^5 years changes the N_2D^+/N_2H^+ ratio only marginally. The difference between the ratios after 10^6 years and 10^5 years is less than 0.01. In models with a evolution time of 10^4 years, the abundances are no longer in equilibrium. In the coldest protostar (20 K), the deuterium fractionation is already high (0.26), but for the warmer objects, the N_2D^+/N_2H^+ ratio is a factor $\sim$2 lower than in chemical equilibrium. Although already quite low, these values still agree with the observations. Evolution times longer than 10^7 years do not change the results, because equilibrium has already been reached.

Another important parameter is the cosmic-ray ionisation rate. In our model, we used $\zeta = 3 \times 10^{17}$ s^{-1} (van der Tak & van Dishoeck 2000). A ζ of 6×10^{17} s^{-1} increases the N_2H^+ abundance by a factor of 1.5, but the deuterium fractionation is lowered by 40%. A cosmic-ray ionisation rate of 1.5×10^{17} s^{-1} increases the N_2D^+/N_2H^+ ratio by 30%.

The central density of the core, hence the envelope mass, has a similar effect on the deuterium fractionation as ζ. In our models, we varied the density to match the observed N_2D^+/N_2H^+ ratio best. The only constraint we put on the central density is that the resulting envelope mass should be a few solar masses. For our best-fit model, we derive an envelope mass of 4.6 $M_\odot$. Decreasing the density by a factor of a half, the deuterium fractionation decreases by 40%. With a density twice as high as our best-fit model, the N_2D^+/N_2H^+ increases by a factor of 1.2.

The last crucial parameter we investigated is the binding energy of CO and N_2 on dust grains. In our model, we used binding energies of 1100 K and 982.3 K for CO and N_2, respectively, which are the binding energies on mixed CO-H_2O ice. We also calculated the models using the values for E_b on pure CO ice (855 and 790 for CO and N_2, respectively, Öberg et al. 2005). With these values, the resulting N_2D^+/N_2H^+ ratios drop to <0.04 for all four temperatures.

6. Summary

We observed 20 Class 0 protostars in N_2H^+ 1–0, N_2D^+ 1–0, 2–1 and 3–2, $C^{18}O$ 1–0 and HCO^+ 3–2. The integrated intensities of the N_2H^+ 1–0 lines in our sample are comparable to those found in prestellar cores (Crapsi et al. 2005). The optical depths are typically 67% lower in the Class 0 sources, but because the excitation temperature is 2–3 K higher and the line width is about 2.5 time larger, the N_2H^+ column densities ($\sim 10^{13}$ cm^{-2}) are also comparable. The presence of a protostar also affects the kinematics of the cores. The N_2H^+ lines are significantly wider in Class 0 sources than in prestellar cores (on average, 0.61 km s^{-1} and 0.26 km s^{-1}, respectively). A comparison of our HCO^+ observations with observations conducted with a $\sim$three times larger beam (Gregersen et al. 2000) leads us to the conclusion that HCO^+ 3–2 stems mainly from a compact region of about 4000 AU in size.

The dependence of the N_2D^+/N_2H^+ ratio on dust temperature, CO depletion factor, and the $L_{BOL}/F_{1.3}^{220\ pc}$ ratio clearly indicates a close relation between deuterium fractionation and evolutionary stage of a Class 0 protostar. For the subsample of sources in the Perseus cloud, the correlation is striking. This migh indicate the influence of the environment on the deuterium fractionation.

The correlation of the deuterium fractionation and the CO depletion factor looks qualitatively like the one found in prestellar cores (Crapsi et al. 2005). However, whereas in prestellar cores, the N_2D^+/N_2H^+ ratio stays low until $f_D(CO) \sim 10$, in protostars, the ratio starts to rise at $f_D(CO) \sim 3$. This difference occurs because CO is highly depleted at the centre of prestellar cores, but not at the centre of protostellar cores.

There is a weak correlation of N_2D^+ line width with N_2D^+/N_2H^+ ratio, but line broadening by multiple sources makes this conclusion suspect. A clear correlation with other kinematical tracers, especially with δv, is found. Sources with a high N_2D^+/N_2H^+ ratio clearly show infall motion ($\delta v \sim -0.4$). The lower the deuterium fractionation gets, the more δv increases. This might reflect the outflow activity increasing with evolutionary stage (Richer et al. 2000).

A model with a power-law density and temperature profile reproduces the correlation between the N_2D^+/N_2H^+ ratio and both T_{Dust} and the CO depletion factor very well. In these models, the protostellar envelopes are chemically stratified. The inner part is too warm for CO to freeze out, so that the N_2H^+ abundance and the deuterium fractionation are low. At radii where the temperature drops below $\sim$20 K, CO is mostly depleted and the N_2D^+/N_2H^+ ratio increases by several orders of magnitude. At even larger radii, the lower density decreases the degree of CO depletion, and thus the N_2D^+/N_2H^+ ratio also decreases.

The results of this work, in combination with the results of Crapsi et al. (2005), show that the deuterium fractionation is highest at the moment of collapse. The primary use of the deuterium fractionation of N_2H^+ is to identify very young protostellar objects, because the decline of the N_2D^+/N_2H^+ ratio is rather steep.

Comparisons of N_2H^+ fractionation with the deuterium fractionation of HCO^+ and NH_3 show clear differences, which are due either to the influence of freeze-out on dust grains, differences in chemical reactions, or both. The low DCO^+/HCO^+ ratio observed by Jørgensen et al. (2004) is a prediction of our model. In young, i.e., cool objects, the NH_2D/NH_3 ratio, observed by Hatchell (2003) is comparable to the deuterium fractionation of N_2H^+. As the temperature increases, the N_2D^+/N_2H^+ ratio falls off much faster than the NH_2D/NH_3 ratio, which stays above 0.15 in all observed objects. This could be due to desorption of deuterium enhanced ammonia from the dust grains.

Acknowledgements. We would like thank the IRAM 30m staff for their assistance during the observations. Furthermore, we gratefully thank L. Pagani for providing us with the Monte-Carlo code. M. Emprechtinger, N. H. Volgenau, and M. C. Wiedner are member of the Nachwuchsgruppe of the Sonderforschungsbereich 494, which is funded by the Deutsche Forschungsgemeinschaft (DFG).

References

Adams, F. C. 1990, ApJ, 363, 578
Aikawa, Y., Wakelam, V., Garrod, R. T., & Herbst, E. 2008, ApJ, 674, 984
Alves, J. F., Lada, C. J., & Lada, E. A. 2001, Nature, 409, 159

André, P., Ward-Thompson, D., & Barsony, M. 1993, ApJ, 406, 122
André, P., Ward-Thompson, D., & Motte, F. 1996, A&A, 314, 625
Aikawa, Y., Wakelam, V., Garrod, R. T., et al. 2008, ApJ, 674, 984
Bacmann, A., Lefloch, B., Ceccarelli, C., et al. 2003, ApJ, 585, L55
Bernes, C. 1979, A&A, 73, 67
Bergin, E. A., & Snell, R. L. 2002, ApJ, 581, L105
Bergin, E. A., Alves, J., Huard, T., et al. 2002, ApJ, 570, 101
Bisschop, S. E., Fraser, H. J., Oberg, K. I., et al. 2006, A&A, 449, 1297
Boogert, A. C. A., Pontoppidan, K. M., Knez, C., et al. 2008, ApJ, 678, 985
Caselli, P., Walmsley, C. M., Terzieva, R., & Herbst, E. 1998, ApJ, 499, 234
Caselli, P., Walmsley, C. M., Tafalla, M., Dore, L., & Myers, P. C. 1999, ApJ, 523, L165
Caselli, P., Benson, P. J., Myers, P. C., & Tafalla, M. 2002a, ApJ, 572, 238
Caselli, P., Walmsley, C. M., Zucconi, A., et al. 2002b, ApJ, 565, 344
Caselli, P., Vastel, C., van der Tak, F. F. S., et al. 2008, A&A, submitted
Ceccarelli, C., & Dominik, C. 2005, A&A, 440, 583
Ceccarelli, C., Loinard, L., Castets, A., et al. 2001, A&A, 372, 998
Černis, K. 1990, Ap&SS, 166, 315
Crapsi, A., Caselli, P., Walmsley, C. M., et al. 2005, ApJ, 619, 379
Crapsi, A., Caselli, P., Walmsley, M. C., et al. 2007, A&A, 470, 221
Dalgarno, A., & Lepp, S. 1984, ApJ, 287, L47
Daniel, F., Dubernet, M.-L., Meuwly, M., et al. 2005, MNRAS, 363, 1083
Enoch, M. L., Young, K. E., Glenn, J., et al. 2006, ApJ, 638, 293
Flower, D. R., Pineau des Forêts, G., & Walmsley, C. M. 2004, A&A, 427, 887
Flower, D. R., Pineau des Forets, G., & Walmsley, M. 2006, 2006, A&A, 456, 215
Fontani, F., Caselli, P., Crapsi, A., et al. 2006, A&A, 460, 709
Fontani, F., Caselli, P., Bourke, T. L., Cesaroni, R., & Brand, J. 2008, A&A, 477, L45
Frerking, M. A., Langer, W. D., & Wilson, R. W. 1982, ApJ, 262, 590
Froebrich, D. 2005, ApJS, 156, 169
Froebrich, D., Smith, M. D., & Hodapp, K.-W. 2003, MNRAS, 346, 163
Fuller, G. A., & Myers, P. C. 1992, ApJ, 384, 523
Gerlich, D., Herbst, E., & Roueff, E. 2002, Planet. Space Sci., 50, 1275
Gregersen, E. M., Evans, N. J. II., Mardones, D., et al. 2000, ApJ, 533, 440
Gueth, F., Bachiller, R., & Tafalla, M. 2003, A&A, 401, 5
Hassel, G. E., Herbst, E., & Garrod, R. T. 2007 [arXiv:astro-ph/0803.1805]
Hatchell, J. 2003, A&A, 403, 25
Hatchell, J., Richer, J. S., Fuller, G. A., et al. 2005, A&A, 440, 151
Herbig, G. H., & Jones, B. F. 1983, AJ, 88, 1040
Jijina, J., Myers, P. C., Adams, & Fred, C. 1999, ApJS, 125, 161
Jørgensen, J. K., Schöier, F. L., & van Dishoeck, E. F. 2004, A&A, 416, 603
Kirk, H., Johnstone, D., & Di Francesco, J. 2006, ApJ, 646, 1009
Kramer, C., Alves, J., Lada, C. J., et al. 1999, A&A, 342, 257
Kramer, C., Richer, J., Mookerjea, B., et al. 2003, A&A, 399, 1073
Kwon, W., Looney, L. W., Crutcher, R. M., et al. 2006, ApJ, 653, 1358
Lacy, J. H., Knacke, R., Geballe, T. R., & Tokunaga, A. T. 1994, ApJ, 428, L69
Lada, C. J., & Wilking, B. A. 1984, ApJ, 287, 610
Lee, J. E., Bergin, E. A., & Evans, N. J., II 2005, ApJ, 631, 351
Looney, L. W., Mundy, L. G., & Welch, W. J. 2000, ApJ, 529, 477
Looney, L. W., Mundy, L. G. & Welch, W. J. 2003, ApJ, 592, 255
Mardones, D., Myers, P. C., Tafalla, M., et al. 1997, ApJ, 489, 719
Maret, S., Bergin, E. A., & Lada, C. J. 2006, Nature, 442, 425
Matthews, B. C., & Wilson, C. D. 2002, ApJ, 574, 822
Millar, T. J., Roberts, H., Markwick, A. J., et al. 2000, RSPTA, 358, 2535
Myers, P. C., & Ladd, E. F. 1993, ApJ, 413, 47
Myers, P. C., Adams, F. C., Chen, H., et al. 1998, ApJ, 492, 703
Öberg, K. I., van Broekhuizen, F., Fraser, H. J., et al. 2005, ApJ, 621, L33
O'Linger, J., Wolf-Chase, G., Barsony, M., et al. 1999, ApJ, 515, 696
Oliveira, C. M., Hebrard, G., Howk, J. C., et al. 2003, ApJ, 587, 235
Pagani, L., Bacmann, A., Cabrit, S., et al. 2007, A&A, 467, 179
Parise, B., Ceccarelli, C., Tielens, A. G. G. M., et al. 2006, A&A, 453, 949
Pineda, J. E., Caselli, P., & Goodman, A. A. 2008, ApJ, 679, 481
Redman, M. P., Rawlings, J. M. C., Nutter, D. J., Ward-Thompson, D., & Williams, D. A. 2002, MNRAS, 337, L17
Richer, J. S., Shepherd, D. S., Cabrit, S., et al. 2000, in Protostars and Planets V, ed. V. Mannings, A. Boss, & S. Russell (Tucson: Univ. Arizona Press), 867
Roberts, H., & Millar, T. J. 2000, A&A, 364, 780
Roberts, H., & Millar, T. J. 2007, A&A, 471, 849
Roberts, H., Herbst, E., & Millar, T. J. 2004, A&A, 424, 905
Saraceno, P., André, P., Ceccarelli, C., et al. 1996, A&A, 309, 827
Schnee, S., Caselli, P., Goodman, A., et al. 2007, ApJ, 671, 1839
Shirley, Y. L.. Evans, N. J. II, Rawlings, J. M. C., et al. 2000, ApJS, 131, 249
Shu, F. H. 1977, ApJ, 214, 488
Smith, M. 1998, Ap&SS, 261, 169
Tafalla, M., Myers, P. C., Caselli, P., et al. 2002, ApJ, 569, 815
Tafalla, M., Myers, P. C., Caselli, P., & Walmsley, C. M. 2004, A&A, 416, 191
Tafalla, M., Santiago-García, J., Myers, P. C., et al. 2006, A&A, 455, 577
Terebey, S., Chandler, C. J., & André, P. 1993, ApJ, 414, 759
Tobin, J. J., Hartmann, L., Calvet, N., et al. 2008 [arXiv:0802.2677]
van der Tak, F. F. S., & van Dishoeck, E. F. 2000, A&A, 358, L79
Velusamy, T., & Langer, W. D. 1998, Nature, 392, 685
Visser, A. E., Richer, J. S., Chandler, C. J., et al. 1998, MNRAS, 301, 585
Volgenau, N. H. 2004, Ph.D Thesis, University of Maryland
Volgenau, N. H., Mundy, L. G., Looney, L. W., et al. 2006, ApJ, 651, 301
Ward-Thompson, D., André, P., & Kirk, J. M. 2002, MNRAS, 329, 257
Willacy, K., Langer, W. D., & Velusamy, T. 1998, ApJ, 507, L171
Wilson, T. L., & Rood, R. 1994, ARA&A, 32, 191
Womack, M., Ziurys, L. M., & Wyckoff, S. 1992, ApJ, 387, 417